Remote Sensing of Environment 281 (2022) 113228

Contents lists available at ScienceDirect

Remote Sensing of Environment

journal homepage: www.elsevier.com/locate/rse

Arctic shrub expansion revealed by Landsat-derived multitemporal vegetation cover fractions in the Western Canadian Arctic

Leon Nill [a,*], Inge Grünberg [b], Tobias Ullmann [c], Matthias Gessner [d], Julia Boike [a,b], Patrick Hostert [a,e]

[a] Geography Department, Humboldt-Universität zu Berlin, Unter den Linden 6, 10099 Berlin, Germany
[b] Geosciences, Permafrost Research, Alfred-Wegener-Institute Helmholtz Centre for Polar and Marine Research, Telegrafenberg A45, 14473 Potsdam, Germany
[c] Institute of Geography and Geology, Physical Geography, University of Würzburg, Am Hubland, 97074 Würzburg, Germany
[d] Institute of Optical Sensor Systems, Sensor Concepts and Applications, German Aerospace Center (DLR), Rutherfordstraße 2, 12489 Berlin, Germany
[e] Integrative Research Institute on Transformations of Human-Environment Systems (IRI THESys), Humboldt Universität zu Berlin, Unter den Linden 6, 10099 Berlin, Germany

ARTICLE INFO

Edited by Dr. Marie Weiss

Keywords:
Tundra
Vegetation change
Shrubification
Greening
Spectral unmixing
Mackenzie Delta

ABSTRACT

Warming induced shifts in tundra vegetation composition and structure, including circumpolar expansion of shrubs, modifies ecosystem structure and functioning with potentially global consequences due to feedback mechanisms between vegetation and climate. Satellite-derived vegetation indices indicate widespread greening of the surface, often associated with regional evidence of shrub expansion obtained from long-term ecological monitoring and repeated orthophotos. However, explicitly quantifying shrub expansion across large scales using satellite observations requires characterising the fine-scale mosaic of Arctic vegetation types beyond index-based approaches. Although previous studies have illustrated the potential of estimating fractional cover of various Plant Functional Types (PFTs) from satellite imagery, limited availability of reference data across space and time has constrained deriving fraction cover time series capable of detecting shrub expansion. We applied regression-based unmixing using synthetic training data to build multitemporal machine learning models in order to estimate fractional cover of shrubs and other surface components in the Mackenzie Delta Region for six time intervals between 1984 and 2020. We trained Kernel Ridge Regression (KRR) and Random Forest Regression (RFR) models using Landsat-derived spectral-temporal-metrics and synthetic training data generated from pure class spectra obtained directly from the imagery. Independent validation using very-high-resolution imagery suggested that KRR outperforms RFR, estimating shrub cover with a MAE of 10.6% and remaining surface components with MAEs between 3.0 and 11.2%. Canopy-forming shrubs were well modelled across all cover densities, coniferous tree cover tended to be overestimated and differentiating between herbaceous and lichen cover was challenging. Shrub cover expanded by on average + 2.2% per decade for the entire study area and + 4.2% per decade within the low Arctic tundra, while relative changes were strongest in the northernmost regions. In conjunction with shrub expansion, we observed herbaceous plant and lichen cover decline. Our results corroborate the perception of the replacement and homogenisation of Arctic vegetation communities facilitated by the competitive advantage of shrub species under a warming climate. The proposed method allows for multidecadal quantitative estimates of fractional cover at 30 m resolution, initiating new opportunities for mapping past and present fractional cover of tundra PFTs and can help advance our understanding of Arctic shrub expansion within the vast and heterogeneous tundra biome.

1. Introduction

The Earth system as a whole has been severely altered by human activity, largely at unprecedented scale and magnitude as well as at risk of irreversible change (IPCC, 2021). The Arctic, in particular, has experienced extensive environmental change, warming at more than

* Corresponding author.
E-mail addresses: leon.nill@geo.hu-berlin.de (L. Nill), inge.gruenberg@awi.de (I. Grünberg), tobias.ullmann@uni-wuerzburg.de (T. Ullmann), matthias.gessner@dlr.de (M. Gessner), julia.boike@awi.de (J. Boike), patrick.hostert@geo.hu-berlin.de (P. Hostert).

https://doi.org/10.1016/j.rse.2022.113228
Received 30 March 2022; Received in revised form 9 August 2022; Accepted 18 August 2022
Available online 9 September 2022

twice the rate of the planetary average due to Arctic amplification (Serreze and Barry, 2011; Post et al., 2019). There is pan-Arctic evidence that sea ice and snow cover extent are declining (IPCC, 2021), permafrost is warming and degrading (Biskaborn et al., 2019), hydrological regimes are changing (Liljedahl et al., 2016), tundra fire frequency and magnitude are increasing (Hu et al., 2015) and plant phenology and composition are shifting (Myers-Smith et al., 2019; Bjorkman et al., 2020). The latter includes extensive tundra shrubification, comprising an increase in biomass, cover, and abundance of Arctic shrub species (Tape et al., 2006; Frost and Epstein, 2014; Myers-Smith et al., 2019). This in turn modifies tundra ecosystem functioning, including energy exchanges, nitrogen cycling, carbon storage and fluxes, as well as biodiversity (Myers-Smith et al., 2011). Shrubification, however, has proven to be heterogeneous across the pan-Arctic (Myers-Smith et al., 2015a), arising from a complex interaction between climate regime and site-specific factors such as active layer thickness, soil moisture conditions, local topography, disturbance events, and herbivory intensity (Martin et al., 2017; Mekonnen et al., 2021). This process is thus not uniform across the pan-Arctic, with some regions exhibiting little to no change in shrub abundance (Jorgenson et al., 2015). Since studies on shrub cover changes are predominantly local, there remains substantial uncertainty on the explicit spatial patterns of shrub cover dynamics across larger scales, while a sound understanding of the dynamics of vegetation composition and structure remains indispensable in order to assess carbon fluxes and climate feedback (Loranty et al., 2011).

Remote sensing offers a unique approach to effectively monitor the vast and remote landscapes of the Arctic tundra biome (Beamish et al., 2020), particularly with long and dense time series of medium resolution imagery provided by the Landsat archive free of charge (Wulder et al., 2019). Most prominently in Arctic contexts, trend analyses based on spectral features and vegetation indices, such as the Normalized Difference Vegetation Index (NDVI), were used to reveal patterns of spectral greening and browning (Beck and Goetz, 2011; Ju and Masek, 2016; Berner et al., 2020), or have been used specifically to identify landscape dynamics and disturbances, often associated with permafrost degradation (Nitze and Grosse, 2016; Fraser et al., 2014b; Nitze et al., 2018; Nill et al., 2019). These satellite-based records suggest that a large proportion of the northernmost landscapes has become greener since the early 1980s, indicated by positive trends of remotely sensed vegetation indices (Myneni et al., 1997; Beck and Goetz, 2011; Park et al., 2016). Since vegetation indices serve as proxies of photosynthetic activity, spectral greening trends have been attributed to increases in plant productivity, height, and biomass (Berner et al., 2020), for instance by linking spectral greening to regional evidence of vegetation change (Fraser et al., 2014a; Frost et al., 2014). Regionally, greening has predominantly occurred in the shrub and graminoid tundra north of the Taiga-Tundra Ecotone (TTE) (Bonney et al., 2018; McManus et al., 2012), with strong variability on the local scale related to site-specific factors controlling shrub growth (Seider et al., 2022). However, spectral indices are limited in their expressiveness, since they do not represent measurements of biophysical properties, nor are derived greening and browning trends associated with unique landscape conditions and dynamics (Myers-Smith et al., 2020). Accordingly, index-based approaches do not allow disentangling the contribution of distinct processes such as shrub growth to observed greening patterns from other vegetation types (Andreu-Hayles et al., 2020; Myers-Smith et al., 2020; Mekonnen et al., 2021).

Remote sensing imagery has also facilitated mapping Arctic land cover (Bartsch et al., 2016; Beamish et al., 2020), ranging from pan-Arctic scale using coarse resolution sensors like the Advanced Very High Resolution Radiometer (AVHRR) (Raynolds et al., 2019), to continental and regional efforts based on Landsat (Schneider et al., 2009; Wang et al., 2020). Contrary to spectral indices, land cover classifications provide thematic information, however, they are constrained by the observational unit of a pixel which almost exclusively represents an integrated signal of several distinct surface materials (Keshava and Mustard, 2002). Since the tundra biome comprises a heterogeneous mosaic of various vegetation types at relatively fine scales (Beamish et al., 2017), classification approaches are inherently limited in capturing this sub-pixel heterogeneity (Lantz et al., 2010b). Furthermore, a large variety of spatio-temporal processes, including the expansion of shrub species, often appear within specified class boundaries rather than constituting a discrete shift to different land cover types (Macander et al., 2017; Suess et al., 2018).

In contrast, estimating continuous cover fractions of distinct surface types at the sub-pixel level can be considered more appropriate at 30 m Landsat scale. Fractional cover is commonly retrieved by either Spectral Mixture Analysis (SMA) or by regression-based unmixing. SMA approaches such as Multiple Endmember Spectral Mixture Analysis (MESMA) rely upon pure endmember spectra representing full coverage of a class and solve a system of linear equations through inversion techniques in order to disentangle the mixed-pixel problem into class fractions (Settle and Drake, 1993; Keshava and Mustard, 2002; Roberts et al., 1998). In contrast, regression-based unmixing utilizes class-wise regression models trained on a great range of fraction values between 0% and 100%. While both approaches allow for incorporating inter- and intra-class spectral variability, MESMA deploys a multitude of single linear mixing models and subsequent model selection on a per-pixel basis (Roberts et al., 1998), whereas regression-based unmixing allows for building single global models per target class. Furthermore, regression-based unmixing enables the use of flexible machine learners, capable of handling a complex feature space and characterised by a good predictive performance (Okujeni et al., 2013). Variants of regression-based unmixing are thus widely used in the realm of fraction cover mapping, including the characterization of urban and rural land cover (Okujeni et al., 2013, 2018; Schug et al., 2018; Priem et al., 2019; Schug et al., 2020), forest cover (Hansen et al., 2013; Senf et al., 2020), Mediterranean shrublands (Suess et al., 2018; Higginbottom et al., 2018) and Arctic land cover in particular (Olthof and Fraser, 2007; Beck et al., 2011; Macander et al., 2017; He et al., 2019).

Although the spectral similarity as well as the fine-scale heterogeneous nature of Arctic plant communities complicate the process of disentangling different land cover types (Beamish et al., 2017), previous studies successfully retrieved fractional cover of major vegetation types for a single point in time based on training data obtained from very-high-resolution (VHR) imagery or field surveys. Olthof and Fraser (2007) used Landsat-7 imagery to retrieve fractional cover of five different land cover types for different sites in northern Canada, by incorporating IKONOS VHR satellite imagery to calibrate and validate their regression models. Similarly, Beck et al. (2011) used IKONOS and SPOT imagery in combination with Landsat data and Random Forest (RF) regression modeling to map shrub fractional cover for the North Slope of Alaska around 2000. Fraser et al. (2011) related the regression-tree models developed by Olthof and Fraser (2007) to trends observed of the NDVI and Tasseled Cap transformations in order to predict expected changes in fractional cover. They associated large scale patterns of greening with an increase in vascular plant cover. Macander et al. (2017) mapped a large variety of Plant Functional Types (PFT) for Arctic Alaska using multi-seasonal Landsat imagery and field observations obtained between 2012 and 2014 for training and validating their models. He et al. (2019) deployed a similar approach with field data from 2012, 2016 and 2017, but focused on three major cover components, namely woody, herbaceous, and nonvascular plants. Riihimäki et al. (2019) constrained their analysis to green vegetation cover, but deployed a multi-sensor approach to up-scale binary classifications of vegetation cover obtained from VHR drone imagery to fractional cover at 3 m (PlanetScope), 10 m (Sentinel-2) and 30 m (Landsat-8) resolution. However, due to the limited availability of field observations in the poorly accessible tundra (Beamish et al., 2020), explicitly assessing shrub cover dynamics beyond spectral indices across space and time remains challenging (Frost et al., 2014).

Accordingly, we address this research need and map the past and

present fractional cover of Arctic shrubs and five other land cover types within the greater Mackenzie Delta Region of the Western Canadian Arctic. We introduce the concept of regression-based unmixing of synthetically generated training data to the realm of Arctic land cover mapping. The method originally developed by Okujeni et al. (2013) relies upon class-wise endmember spectra to generate synthetic continuous training data. This allows for creating a broad range of training fractions that can be used in combination with image features and regression modeling to predict the fractional cover of various surface components (Okujeni et al., 2013). Since the pure endmember spectra can be obtained directly from the imagery (*image endmembers*), it offers great potential for mapping the vast and poorly accessible landscapes of the tundra biome. By explicitly integrating image spectra over the entire observational period, we create class-wise multitemporal regression models that enable retrieving fractional cover for six aggregated time periods between 1984 and 2020. Specifically, we addressed the following research questions:

1. How accurately can Arctic shrub and other land cover fractions be mapped using Landsat and regression-based unmixing of synthetic training data?
2. What are the spatio-temporal patterns of land cover fractions within the greater Mackenzie Delta Region?
3. Does the approach explicitly capture shrub expansion in the area since the mid-1980s?

2. Study area

Our study area is situated in the greater Mackenzie Delta Region of the western Canadian Arctic (Fig. 1). It stretches from the outskirts of the Brooks Range in the west (140°W) to the lowlands of the Tuktoyaktuk-Peninsula in the east (130°W), and from the subarctic Richardson Mountains and Anderson Plain in the south (67°N) to the coastal tundra at the Beaufort Sea (70°N). The study area thus encompasses an area of 143,100 km^2 at the transition of subarctic taiga and low arctic tundra, almost exclusively underlain by continuous permafrost. The subarctic divides into the ecozones of the mountainous Taiga Cordillera in the west and the low-lying Taiga Plains in the central and eastern section of the study area. The Mackenzie River forms an alluvial plain consisting of several meandering channels which - bound by the Richardson Mountains and Caribou Hills - empty into the Beaufort Sea (Goulding et al., 2009). The low Arctic tundra predominantly features subtle topography

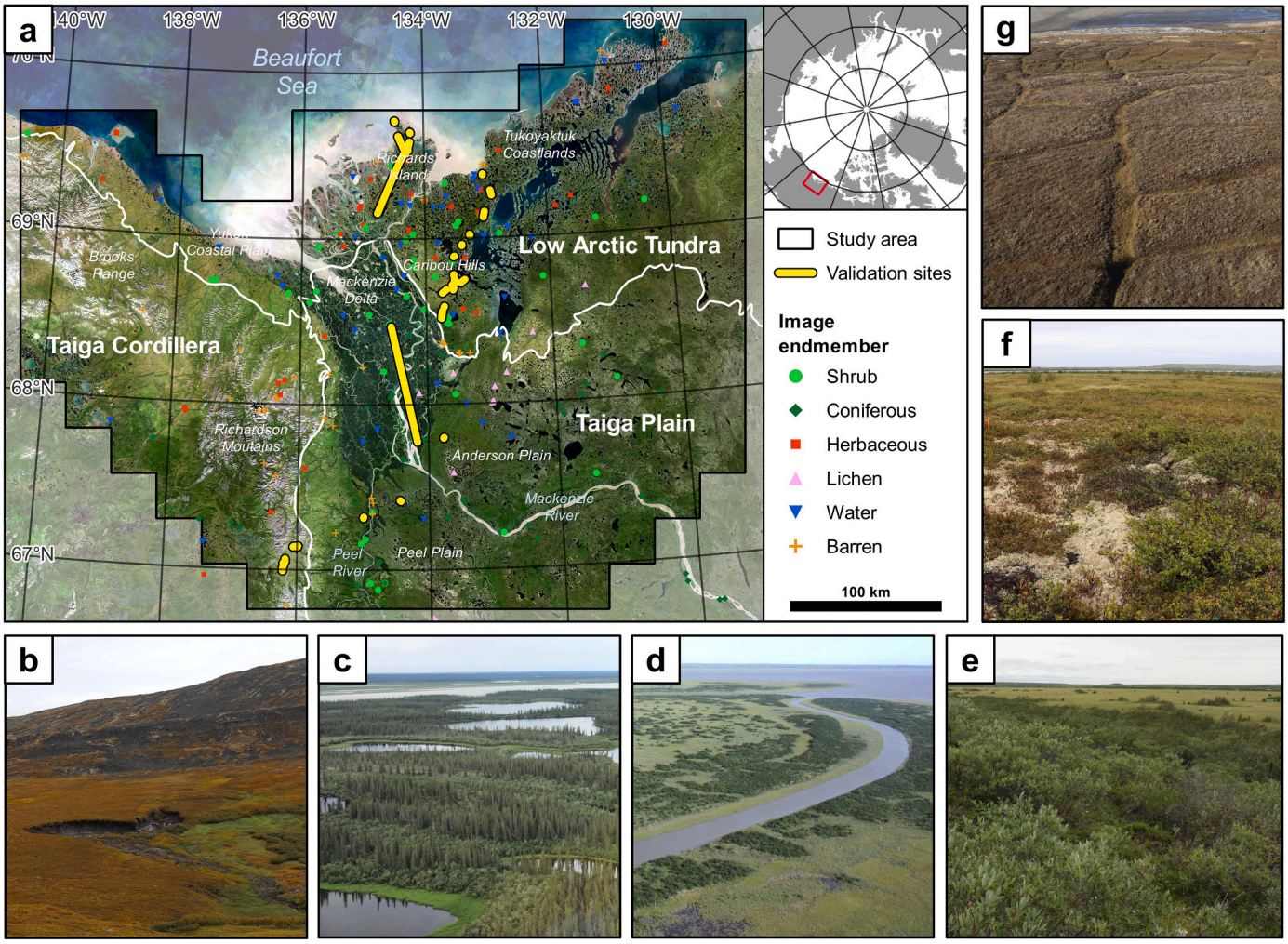

Fig. 1. Map of the Mackenzie Delta Region in the Western Canadian Arctic (a). Overlain are the three major ecoregions (white, Ecological Stratification Working Group (1996), https://sis.agr.gc.ca/cansis/nsdb/ecostrat/gis_data.html, accessed 2022-01-07), the validation sites with available drone and airborne imagery (yellow) and the locations of the endmember pixels. Large-scale patterns of vegetation communities and land cover following topography and latitude include elevated grounds with graminoids and barren surfaces (b), wetland complexes with sequences of sedges, deciduous shrubs/trees and coniferous spruces in the delta (c-d), shrub dominated tundra (e) intermixed with herbaceous vegetation and non-vascular lichens (f), as well as herbaceous and non-vascular dominated polygonal tundra (g) (Image courtesy to T. Ullmann and J. Kunz). (For interpretation of the references to colour in this figure legend, the reader is referred to the web version of this article.)

with rolling hills, numerous depressions filled with thermokarst lakes and wetlands, as well as hummocky and polygonal terrain in the northern parts (Burn and Kokelj, 2009). The Yukon Coastal Plains in the west are further characterised by well-drained upland tundra landscapes, punctuated with erosion valleys leading towards the coastal wetlands. The climate of the Mackenzie Delta Region can be described as cold and dry with a pronounced seasonality of temperature and precipitation. Notable differences arise from the latitudinal position, topography, and proximity to the coast (Burn and Kokelj, 2009). Accordingly, mean annual air temperatures and precipitation (1981–2010) drop from −7.3°C and 297.7 mm in Fort McPherson in the south to −10.1°C and 160.7 mm in Tuktoyaktuk at the coast (Environment Canada, 2021). Climate also determines the large scale prevalent composition and structure of vegetation communities, where the dense coniferous forests of the boreal south are gradually replaced by shrub tundra communities with increasing latitude (Timoney et al., 1992). The region has warmed by >2.5 °C since 1970 (Burn and Kokelj, 2009), which presumably has caused an extensive greening of the surface driven by the expansion of - predominantly deciduous - shrub species (Lantz et al., 2010a; Fraser et al., 2014a; Nill et al., 2019).

To characterise the patterns and dynamics of the vegetation cover, we differentiated among four different Plant Functional Types (PFTs) that in their various combinations make up the vegetation communities found in the study area. Grouping species into PFTs allows to abstract from the species level to a more general framework while accounting for similar ecological functions and environmental responses to change within the groups (Chapin et al., 1996). Accordingly, we identified the following classes:

1. *Shrub* – comprises deciduous woody vegetation and evergreen shrubs. Shrubs are common throughout the study area, dominating in the lake rich lowlands, along streams and rivers, and as pioneer species in alluvial settings or following wildfire disturbance (Burn and Kokelj, 2009; Moffat et al., 2016; Lantz et al., 2010a). This class consists mostly of the genera willow (*Salix*), birch (*Betula*) and alder (*Alnus*). We did not differentiate between tall deciduous shrubs and deciduous trees, as – from a remote sensing perspective – they are spectrally identical and the tree-shrub differentiation is gradual and subject to definition. Furthermore, we focused on the shrub dominated low Arctic landscapes where a cover expansion is driven by species not reaching the height of trees. Patches of tall shrubs are often formed by green alder (*Alnus viridis*) which commonly grow a few meters apart on undisturbed sites while they form a dense cover in combination with willows (e.g. *Salix pulchra*, 1d–e) after fire events (Lantz et al., 2010a). Willows also prevail in riparian landscape settings (Grünberg et al., 2020). In the shrub tundra, dense canopies of low statue shrubs (20–50 cm) are often formed by American dwarf birches (*Betula glandulosa*) accompanied by shorter ericaceous shrubs of the genera *Rhododendron* and *Vaccinium* (Lantz et al., 2010a; Grünberg et al., 2020) (Fig. 1f).
2. *Coniferous* – encompasses mostly black spruce (*Picea mariana*) and white spruce (*Picea glauca*) trees (Lantz et al., 2010a). Dominating in large parts of the boreal south, their presence declines with latitude until they are only found as isolated patches on favourable grounds (Scott and Hansell, 2002). In the delta, the thermal regime permits the treeline to stretch further north and spruces typically establish on grounds that were elevated above the annual flooding level (Burn and Kokelj, 2009) (Fig. 1c). With time, the vegetation community consisting of spruces, alders, and bearberries, develops towards an open spruce forest with a thick lichen and moss layer (Pearce et al., 1988).
3. *Herbaceous* – includes graminoids, forbs and ferns. They form an integral part of shrub tundra formations and the understory vegetation in open spruce forests. Sedges (mostly *Carex* spp. and *Eriophorum* spp.) populate poorly drained areas while drier parts are favourable for grasses (Burn and Kokelj, 2009). Accordingly, wetlands are often dominated by tussock-forming sedges while grasses populate well-drained hilltops (Fig. 1b, d, g).
4. *Lichen* – represents the only separated nonvascular component. The most abundant species are *Cladina rangiferina* and *Cladina stellaris* (Fraser et al., 2014a). They are mostly inter-mixed within shrub tundra (Fig. 1f) or build a thick layer with mosses in open spruce woodlands (Fraser et al., 2014a; Pearce et al., 1988). Although lichens are often grouped together with mosses as non-vascular PFTs, they differ substantially in their spectral appearance, complicating a combined classification. Apart from that, we could not delineate pure moss pixels as this class is generally mixed with all other cover types. Generally, lichens and mosses are virtually ubiquitous in the landscape and thus likely to be particularly included in our herbaceous class.

Complementing the four PFTs, we further included two non-vegetation classes:

5. *Barren* – encompasses rock outcrops, open-soil (e.g. alluvial and coastal sandbars) and artificial built-up surfaces such as roads.
6. *Water* – describes all varieties of open water bodies, including deep lakes and sediment-rich streams and rivers. Although permanent water bodies were masked prior to the analysis of six the time frames, we included this class to account for its spectral influence in regions such as wetlands or small streams within mixed pixels.

3. Methods

The estimation of Landsat-based multitemporal land cover fractions comprised a sequence of methodological building blocks (Fig. 2). First, we created a wide array of image features from preprocessed Landsat Collection 2 image time series for each of six time intervals. These intervals were 1984–1990, 1991–1996, 1997–2002, 2003–2008, 2009–2014 and 2015–2020. Second, we developed an image endmember library by identifying pure, temporally stable land cover pixels and extracting their band-wise spectral reflectance from the image features. Third, we generated synthetic training data based on the endmember library which served as input for the class-wise regression models. Then, the final fraction cover maps for each cover class, target time frame and regression algorithm were derived by averaging the prediction results of twelve individual model runs. We assessed the reliability of our results by validating the predictions for the most recent 2015–2020 interval using manually derived reference fractions based on the visual interpretation of VHR airborne and drone imagery obtained during field campaigns in 2018/2019. Following the validation, we assessed the spatial patterns and temporal dynamics of the land cover fractions in the Mackenzie Delta Region.

3.1. Image processing

3.1.1. Landsat data

We retrieved all available Landsat Thematic Mapper (TM), Enhanced Thematic Mapper (ETM+) and Operational Land Imager (OLI) Collection 2 Level-1 images between 1984 and 2020 with a maximum cloud cover of 70% from the United States Geological Survey (USGS) using the USGS/EROS machine-to-machine API (https://m2m.cr.usgs.gov/, accessed 2021-02-09). Collection 2 marks the second major collection of the Landsat archive which most notably comes with an improvement in the absolute geometric accuracy of the image data (U.S. Geological Survey, 2021). We incorporated all scenes between April and October into the search, covering early-spring to end-of-autumn resulting in a total of 10,640 Landsat scenes covering 36 Worldwide Reference System-2 (WRS-2) path/rows (Fig. 3). The high-latitudinal location of the study area results in significant overlap between the individual WRS-2 paths of the satellites, which in turn improves acquisition frequency and counteracts the high incidence cloud cover and generally short seasonal window suited for optical remote sensing in Arctic

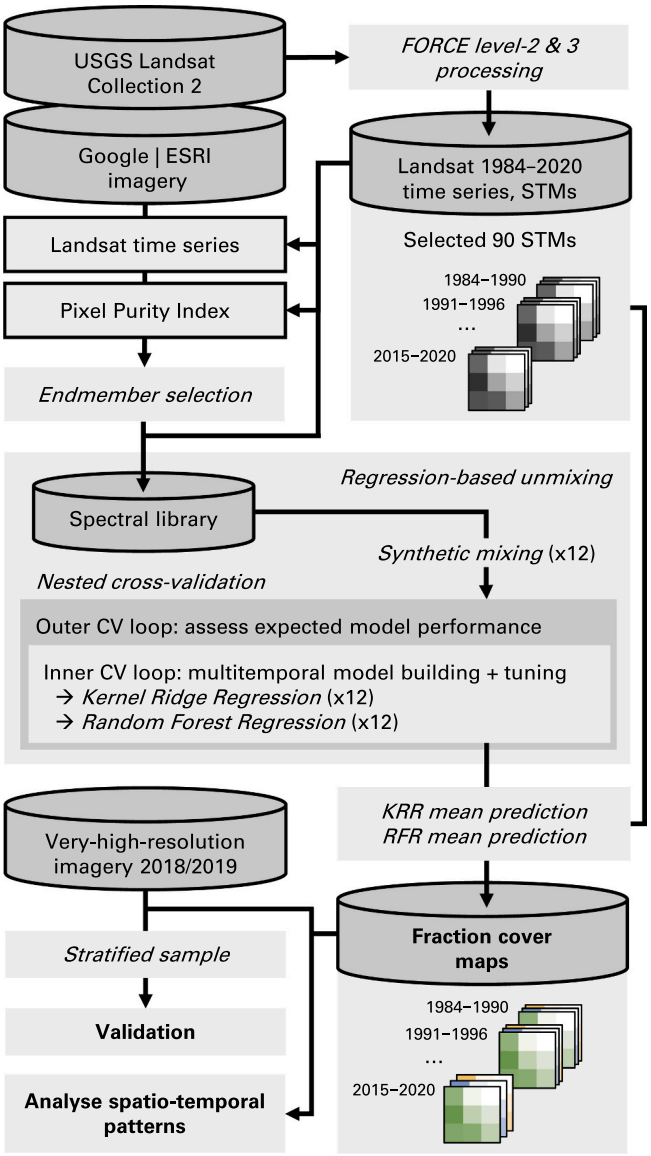

Fig. 2. Methodological workflow for estimating fractional cover based on Landsat imagery and regression-based unmixing of synthetically generated training data.

environments. However, the number of per-pixel clear-sky-observations (excluding cloud, cloud shadow, snow, and saturated pixels) is heterogeneous across space and differs between the six target time intervals (supplementary materials A).

For preprocessing the level-1 imagery as well as for the creation of the higher level image products, including analysis-ready-data, we applied the Framework for Operational Radiometric Correction for Environmental monitoring (FORCE) (Frantz, 2019). Preprocessing the level-1 imagery to level-2 data encompassed masking clouds, cloud shadows and snow or ice, and correcting radiometric effects including atmospheric, topographic, BRDF and adjacency effect correction (Frantz et al., 2016). The needed auxiliary data encompassed the 30 m resolution Copernicus Digital Elevation Model (GLO-30) and a pre-compiled water vapor database during atmospheric correction (Frantz et al., 2019). FORCE allowed for the efficient handling of large data volumes through the creation of data cubes after reprojecting the imagery into a common coordinate system. Here, we used the EPSG:3573 coordinate system with an adjusted central meridian to match the center location of the study area.

Our analyses covered the six aggregated time periods 1984–1990, 1991–1996, 1997–2002, 2003–2008, 2009–2014 and 2015–2020. For each of these intervals, we collapsed all available clear-sky-observations (CSOs) at the pixel-level into a single (artificial) year, maintaining the day-of-year (DOY) position in time of the respective observations (supplementary materials B). We deemed this necessary given the comparably sparse intra-annual observation density in the earliest two decades, while a high observation density greatly improves the quality and consistency of image features derived from the time series. Unlike for aggregated time periods, the quality and accuracy of predictions from single years would be largely governed by the respective data availability. However, our approach of multi-annual time series aggregation implies that abrupt land surface change triggered by disturbance events is smoothed. While detecting such events at scales smaller than six years is thus impossible from our data, long-term effects of disturbance are nevertheless captured. Importantly, the key process of interest in our study - shrub expansion - develops gradually and does not necessarily require annual assessments for monitoring. With a distance of on average six years between the aggregated periods, we ensured that changes in shrub abundance are still captured at relatively fine temporal scale.

In order to ensure a consistent, gap-free time series in which potential noise of remaining image artifacts (e.g. cloud remnants) is suppressed, while the spectral-temporal variability of the time series is maintained, we interpolated the aggregated level-2 time series into an equidistant (8-day) smoothed time series using an ensemble of Radial Basis Function (RBF) kernels with varying widths of the Gaussian bell (σ= 8, 16 or 32 days) (supplementary materials B) (Frantz, 2019; Schwieder et al., 2016). Larger widths lead to stronger smoothing and reduce the chance of gaps in the time series. Smaller widths result in a smoothing much closer to the actual raw time series, but the chance of data gaps increases. By deploying an ensemble of RBF kernels with varying widths, each kernel was weighted in proportion to the prevalent data density of the raw time series, resulting in an adaptive degree of smoothing based on actual data availability.

3.1.2. Spectral-temporal metrics

The processed level-2 imagery then served as input within the

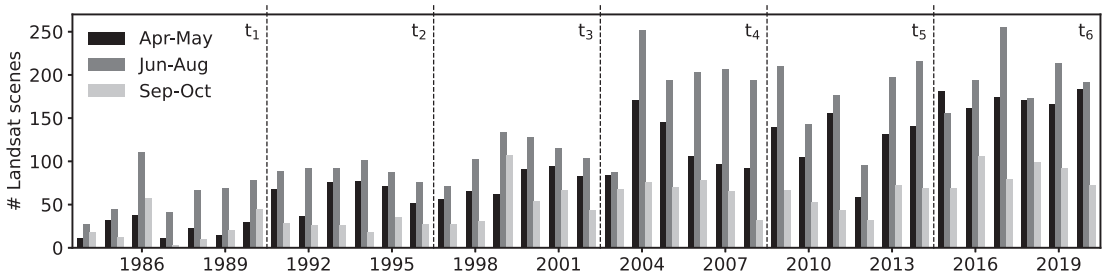

Fig. 3. Number of Landsat scenes with <70% cloud cover between 1984 and 2020. Seasonal windows are grouped together and dashed vertical lines indicate borders between the six target time intervals. See supplementary materials A for pixel-wise maps of clear-sky-observations.

higher-level processing suite of FORCE to derive Spectral-Temporal-Metrics (STM) for each time interval. STMs constitute a dimensionality reduction by calculating pixel-wise statistics (e.g. mean, standard deviation) of individual bands that preserve or may even amplify the variance of the image time series and highlight seasonal characteristics of different land cover types (Müller et al., 2015). STMs were retrieved for an array of various temporal, spectral and statistical combinations: First, we considered three intra-annual time intervals: The entire season (DOY 91–305), as well as the first- (DOY 100–200) and second-half (DOY 200–300) of the season. The underlying assumption of such a differentiation is that differences in phenology between the cover types become amplified by targeting distinct phenological windows (He et al., 2019; Macander et al., 2017; Okujeni et al., 2021). Second, a wide range of input spectral bands, indices and transformations were included. This encompassed the original six Landsat spectral bands (BLU, GRN, RED, NIR, SW1, SW2), the Tasseled Cap components greenness (TCG), brightness (TCB) and wetness (TCW) (Crist, 1985), the Normalized Difference Vegetation Index (NDVI) (Tucker, 1979), the Normalized Difference Moisture Index (NDMI) (Gao, 1996) and the modified Normalized Difference Water Index (MNDWI) (Xu, 2006), as well as the Normalized Burn Ratio (NBR) (Key and Benson, 2006) and the Enhanced Vegetation Index (EVI) (Huete et al., 2002). Third, we calculated a set of 11 statistical metrics, namely the minimum, several quartiles (10th, 25th, 50th, 75th, 90th), the maximum, mean, standard deviation, range, and the inter-quartile range. In total this comprised an initial set of 462 STMs per target time interval. We visually assessed the initial predictor pool and removed all features exhibiting noisy patterns in any of the target intervals. The noise could mostly be attributed to image artifacts introduced by unmasked (cirrus) cloud remnants, thus statistical metrics highlighting spectral extremes and ranges (e.g. maximum, range) were excluded most frequently. Ultimately, this reduced the dimensionality to 90 bands (supplementary materials C).

3.2. Fraction cover modeling using regression-based unmixing

We deployed regression-based unmixing to map the cover fractions of shrubs, coniferous trees, herbaceous plants, lichens, water and barren surfaces for each time interval. Regression-based unmixing combines training data representing continuous fractions of the cover types with spectral bands or image features in order to build class-wise regression models (Okujeni et al., 2013; Schug et al., 2020). We introduced the concept of regression based-unmixing using synthetically-generated training (hereafter: *synthmix*) developed by Okujeni et al. (2013) to the realm of Arctic land cover mapping. This allowed for efficiently acquiring representative training fractions solely based upon the construction of a spectral library containing image-based spectral signatures of pure surfaces. Using *synthmix*, continuous land cover fractions were generated synthetically by combining the pure spectral signatures, or *endmembers*, of the library in a linear fashion (Okujeni et al., 2013). Based on the synthetic training data, we trained class-wise regression models and predicted fractional cover into space for each of the time intervals. To include a wide array of mixtures and improve prediction accuracy, we repeated this process twelve times and obtained the final fraction cover maps using ensemble averaging.

3.2.1. Spectral library development

We identified pure image endmembers at Landsat 30 m pixel scale for all six target classes (Fig. 1). The goal was to create a multi-annual endmember library consisting of pure surfaces representative for the entire study period (1984–2020), thus enabling the model's applicability across time and accounting for the temporal spectral variability of the classes. The latter may arise from shifts in climatic conditions and phenology as well as differences among the Landsat sensors (Suess et al., 2018; Okujeni et al., 2021). Endmember candidates had to comply with certain criteria: First, we used Landsat time series and linear trend analysis of selected bands and indices to identify pixels exhibiting spectral stability, thus showing no obvious signs of disturbance or gradual processes such as greening and browning. Second, VHR imagery was used to visually interpret characteristics of the surface cover regarding structure, texture and colour. This was combined with drone and airborne imagery to better understand the expression of certain surface types in the relatively coarser Google/ESRI images. Third, we used STMs describing the median of the spectral bands for the six target intervals to calculate a multi-temporal Pixel Purity Index (PPI) (Chang and Plaza, 2006). The PPI is a data-driven technique to highlight pure pixels in the input imagery, while pure is defined as a multi-dimensional data point being at the borders of the feature space (Chang and Plaza, 2006). In summary, the median image stack was transformed using Minimum Noise Fraction (MNF) which essentially yields the Principal Components with steadily increasing noise levels (Green et al., 1988). From this, we randomly generated 5000 vectors in this feature space (*skewers*) on which the MNF-transformed data points were projected, each time highlighting and flagging the most distant 0.5% data points. Finally, we created a heat map of the number of times a pixel was flagged as extreme and thus potentially pure.

Based on these three main criteria, we compiled the locations of endmembers for the spectral library while accounting for intra-class spectral variability. Accordingly, we sampled point locations scattered throughout the study area (Fig. 1), while refraining from selecting pixels within the extent of drone and airborne imagery used for validation. Endmember pixels of each class were labeled as 100% surface cover although it could not be ruled out that a small remaining fraction was influenced by other cover types. In consideration of the observation-scale (30 m × 30 m), the small-scale heterogeneity of tundra vegetation communities, and the fact that ambiguities were greatest between non-shrub classes (e.g. pure herbaceous without lichen or moss cover), we, like previous studies, regarded this as an acceptable limitation of the approach (Suess et al., 2018; Okujeni et al., 2021).

In total, we identified 287 pure pixel locations, summing to 67 for shrub, 68 for coniferous, 41 for herbaceous, 22 for lichen, 41 for water, and 48 for barren/built-up. Since the STM spectrum at each endmember location was extracted for all six target time intervals, this yielded a final endmember library with 1722 entries. Exemplary spectra showing the median STM for the entire season are shown in Fig. 4.

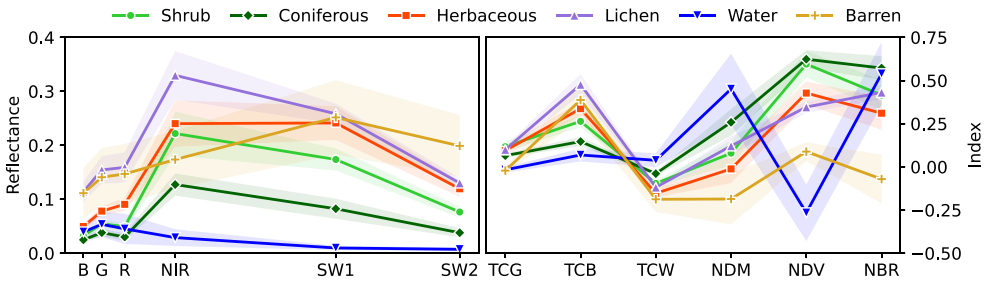

Fig. 4. Average endmember spectra (±1 standard deviation depicting intra-class variance) derived from all six target intervals (1984–2020) representing the median STM of the six spectral bands and indices for the entire season (DOY 91–305) of each class.

3.2.2. Generation of synthetic training data

For each land cover class and individual model run, continuous training fractions were generated by creating randomized linear mixtures of different endmember spectra between 0% and 100%. The generated target class' fraction of the respective mixture represents the output to be estimated by the model. The process of creating linear mixtures is built on the physical assumption that a mixed pixel represents a linearly weighted combination of the pure spectra of its individual components (Settle and Drake, 1993). Originally, an endmember library is composed of actual reflectance spectra (e.g. Landsat bands), but the strength of using artificial image features such as STMs has been demonstrated in the context of mapping urban-rural land cover (Schug et al., 2020) and diverse vegetation classes in California (Okujeni et al., 2021). Accordingly, our spectra in the endmember library were composed of the STM values of each time interval at the 287 endmember locations.

A single run of *synthmix* was applied for each class and model to generate 2500 synthetic training data points. Overall, the parameter setup of *synthmix* followed the proven strategy of previous studies (Okujeni et al., 2017, 2018; Schug et al., 2020), in which each synthetic training instance was generated as follows: First, we specified the possible number of unique endmember spectra that make up the mixed signal, each associated with a unique probability (p) of occurrence. This encompassed binary ($p = 0.70$), ternary ($p = 0.25$) and quaternary ($p = 0.05$) mixing ratios. Second, after the random choice of the mixing ratio (two, three or four), an endmember spectrum of the target class was randomly selected, followed by filling up the remaining slots (one, two or three) with randomly drawn spectra using the proportional occurrence of class entries in the database. Here, we allowed for inter-class and intra-class mixtures. Third, random mixing weights between 0% and 100% were generated, relating to the fraction of each drawn spectrum in the final synthetic signal. These were iteratively generated for each spectrum under the constraint of summing to 100%. Last, the synthetic feature was created by linearly weighting the input spectra based on the fraction weights, while the associated mixing fraction of the target class' spectra represented the continuous training fraction. The original pure endmember spectra of the target class (100% cover) and other classes (0% cover) were also included in the final training dataset. We post-processed the training data to ensure an equal distribution of cover fractions.

3.2.3. Model building

We deployed Kernel Ridge Regression (KRR) and Random Forest Regression (RFR) to estimate fractional cover, thus incorporating two different approaches of statistical learning. For that, we used the *scikit-learn* implementations of KRR and RFR in Python. Both methods are frequently used in remote sensing classification and regression problems, including fraction cover mapping (Okujeni et al., 2014), stemming from their ability to efficiently handle a high-dimensional, diverse input feature space and capturing non-linearities in the data (Lary et al., 2016; Maxwell et al., 2018).

We applied Bayesian optimisation using a Gaussian Process (see e.g. (Rasmussen and Williams, 2006)) for tuning the hyperparameters of KRR and RFR by making use of the *scikit-optimize* library in Python. This allows to efficiently identify optimal configurations of hyperparameters (Snoek et al., 2012), significantly outperforming standard methods including grid search (Bergstra et al., 2011; Snoek et al., 2012). For this, Gaussian Process Regression is used as a surrogate model to approximate the objective function to be minimized by iteratively sampling and evaluating points in the function space (Snoek et al., 2012). We chose the cross-validated Mean Absolute Error (MAE) as the objective function to be minimized by the Gaussian Process.

RFR is comparably insensitive to parametrize and it is recommended to set the number of trees to a large, while computationally feasible number. Tuning the number of random variables considered at each decision node seems to have the most notable influence on model performance (Probst and Boulesteix, 2018; Probst et al., 2019). Accordingly, we set the number of trees to 1000 and tuned the number of random variables considered at each split (*max_features*), the maximum depth of the tree (*max_depth*), the minimum number of samples required to split an internal (*min_samples_split*) as well as a leaf (*min_samples_leaf*) node. KRR, in turn, is highly sensitive to parametrization. Model building required tuning the strength of regularization α (equivalent to C parameter in Support Vector Machines) and the γ parameter of the RBF kernel specifying the distance by which single data points influence others.

The entire model building process was embedded within a nested cross-validation (CV) scheme (see Fig. 2), which is the preferred choice to counteract selection bias and overly optimistic estimates of model performance (Hastie et al., 2009). Nested CV consists of an inner CV-loop responsible for hyperparameter tuning and model selection, nested within an outer CV-loop in which the expected model performance and building strategy can be assessed. To include a wide array of synthetically generated STM mixtures and improve the predictive performance (Okujeni et al., 2017), we repeated the modeling process twelve times and obtained the final fraction cover maps for each algorithm (KRR & RFR) using ensemble averaging.

3.3. Validation of fraction cover maps

We conducted an internal assessment of model performance as well as an independent validation of the fraction maps. First, 10-fold nested CV provided a baseline of expected model performance, using synthetically generated test sets based on unseen endmember spectra not used in the respective training sets. The independent validation of the fraction maps was based on the visual interpretation of VHR imagery. This is a common validation approach in fraction cover studies (Schug et al., 2018; Suess et al., 2018; Baumann et al., 2018; Schug et al., 2020; Senf et al., 2020; Cooper et al., 2020) and in our case comprised drone and airborne image acquisitions obtained along a latitudinal gradient in 2018/2019, thus enabling the validation of the recent 2015–2020 predictions. We could not realize an independent assessment for each time interval since suitable reference imagery or extensive field observations are not available. We regarded the validation of the recent predictions to function as a surrogate assessment for the entire period, since we trained class-wise multitemporal models based on spectra from the entire study period. Thus, the spectral signals across the entire study period are integrated and noise introduced by seasonality, climate trends and sensor properties are factored in. The applicability of multitemporal regression-based unmixing models has been shown in the context of Mediterranean shrublands (Suess et al., 2018), urban development (Schug et al., 2018) and characterising forest types (Senf et al., 2020). Following the independent accuracy assessment, we assessed the distribution of the pixel-wise fraction cover sum of the individual classes. As the class-wise models are completely independent from one another, systematic biases in single time intervals should result in mismatches between the distributions.

For the independent validation we used drone and airborne imagery. The drone acquisitions were acquired on site in August 2018 and August 2019, using a RGB camera mounted on a DJI Phantom 3. These acquisitions differ in their spatial coverage (0.03–0.16 km^2), ground resolution (0.4–8 cm) and image quality. The airborne orthophotos were acquired by the Modular Aerial Camera System (MACS) on board the Polar-5 airplane in August 2018. The MACS camera was developed by the German Aerospace Center (DLR), Institute of Optical Sensor Systems, Berlin, Germany (supplementary materials D). This included multiple images stratified throughout the study area with a ground resolution of 10–15 cm covering the visual and near-infrared region of the electromagnetic spectrum. The locations of the drone and airborne image mosaics are depicted in Fig. 1.

Validation pixels were selected based on a stratified random sampling approach (Olofsson et al., 2014). The strata for random sampling

were derived by reclassifying the fraction maps of each class into four bins of 25%, thus 0–25%, 25–50%, 50–75%, 75–100%. For each class-wise fraction bin, we randomly sampled up to 9 validation points if the VHR imagery actually included the respective bin range of the classes. To capture the full variety of surface compositions, we manually added 40 points. To account for spatial-auto-correlation, all points were sampled with at least 60 m distance from another while the large majority of points were isolated at >500 m distance. Reference fractions were obtained by labeling the underlying land cover class at the center of a cell of a 9 × 9 grid within each Landsat pixel and subsequently calculating the proportional prevalence of each class (Fig. 5). We ensured the validity of the interpreted references by cross-checking individual interpretations among three persons and removed 27 reference sites where the class assignment was ambiguous due to image border artifacts. In summary, this resulted in a final reference pool of 216 validation pixels at 30 m Landsat scale.

3.4. Identifying spatio-temporal dynamics of Arctic land cover fractions

Prior to analysing the fraction cover maps, we masked permanent water surfaces based on a manually defined decision tree and validated the binary water mask using an area-adjusted stratified random sampling approach (Olofsson et al., 2014) (supplementary materials E). For the spatial analysis, we summarised the fraction cover distribution of each class across three major ecozones and the six observation epochs. To assess the temporal development of each land cover class, we calculated pixel-wise rates of change based on a linear model. We accepted the simplification of using a linear model since we were interested in estimating net average rates of change between 1984 and 2020, acknowledging that change includes non-linear surface dynamics and our multi-annual aggregation collapses the 1984–2020 time series into six observational periods. Previous work has demonstrated the applicability of such an approach for assessing woody cover encroachment at continental scale (Venter et al., 2018). We reduced the impact of prediction uncertainty and spurious effect size by treating change trajectories within the expected margin of error based on the class-wise MAEs to exhibit zero change:

$$\Delta FC_k{}^{-year} = \begin{cases} a + b \times t, & \text{if } |\Delta FC_{k_{1984-2020}}| > MAE_k \\ 0, & \text{otherwise.} \end{cases} \quad (1)$$

where FC_k is the fractional cover of land cover class k, intercept a, slope b and t encoded as years since the first central year from the individual time periods ($t \in \{0, 6, 12, \ldots, 30\}$), and MAE_k is the mean absolute error of class k retrieved from the independent validation procedure. We refrained from filtering criteria based on null-hypothesis significance testing, since b-estimates deemed non-significant based on arbitrarily set p-value thresholds not only included subtle estimated changes centered around zero effect size, but also lead to falsely rejected change trajectories we consider meaningful. Based on the average rates of change, we then assessed fraction cover change across latitudinal gradients of the study region and examined temporal trajectories for a variety of surface conditions.

4. Results

4.1. Accuracy of regressed land cover fractions

All model combinations of algorithm (KRR, RFR) and target class converged well to an optimal solution using Gaussian Process based hyperparameter tuning. Internal CV prospected potentially good predictive performance across all classes (MAEs 4.9–11.3%), while KRR consistently outperformed RFR in its predictive power (Table 1). The independently conducted accuracy assessment using 216 validation pixels labeled with a 9 × 9 grid revealed an overall good predictive capacity of the class-wise multi-temporal KRR model ensembles (Table 1, Fig. 6). We found KRR to outperform RFR also during the independent accuracy assessment and therefore selected the KRR models for our subsequent analyses. MAEs ranged between 3.0 and 11.2% among the target classes: For our main target class, shrubs, we found good agreement between predicted and observed fractions with a MAE of 10.6% and small prediction bias of −1.0%, thus exhibiting a slight underestimation of prevalent shrub cover. Likewise, coniferous tree cover was mapped with a MAE of 10.6%, though with an almost

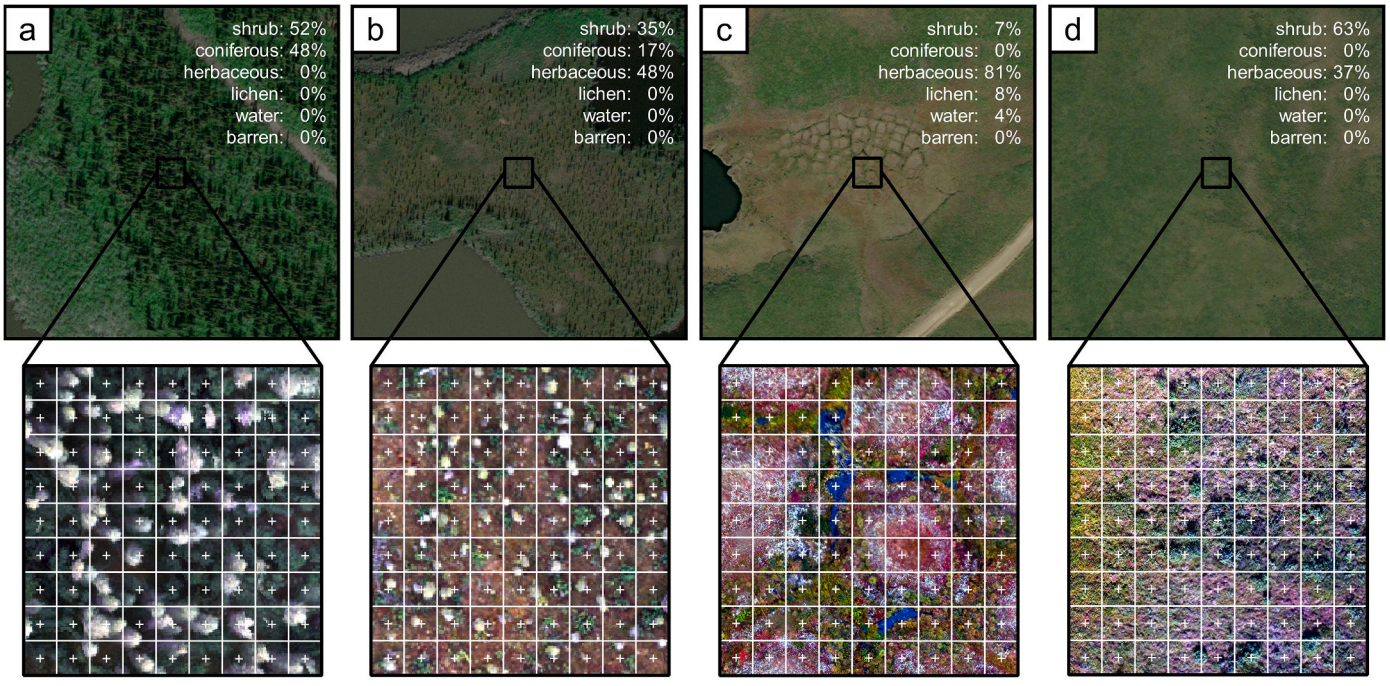

Fig. 5. Example images showing the applied 9 × 9 point grid scheme used in combination with MACS (a & b) and drone (c & d) imagery to validate fraction cover predictions.

Table 1
Accuracy metrics for each class and model obtained from internal and independent accuracy assessment.

Class	Model	Nested cross-validation		Independent validation	
		MAE (%)	Prediction bias	MAE (%)	Prediction bias
Shrub	KRR	6.6 ± 0.7	−1.0 ± 1.0	10.6	−1.0
	RFR	8.7 ± 0.4	−0.3 ± 1.0	13.8	3.6
Coniferous	KRR	4.9 ± 0.4	−0.2 ± 0.6	10.6	10.5
	RFR	7.2 ± 0.4	0.7 ± 0.8	17.5	16.4
Herbaceous	KRR	9.6 ± 0.8	−2.1 ± 1.0	11.2	5.4
	RFR	11.3 ± 0.6	−0.9 ± 0.6	13.0	4.9
Lichen	KRR	6.9 ± 1.7	−1.0 ± 2.0	5.9	5.0
	RFR	8.3 ± 1.4	0.8 ± 2.4	11.2	9.8
Water	KRR	6.6 ± 0.8	−2.2 ± 1.7	3.0	−0.3
	RFR	6.8 ± 0.4	−0.8 ± 1.2	5.1	1.9
Barren	KRR	6.7 ± 0.8	−1.6 ± 0.9	7.3	5.1
	RFR	7.3 ± 0.4	0.0 ± 0.7	10.0	6.8

exclusive positive prediction bias of +10.5%. The bias was present at all tree cover densities. Trees were predicted by the model in tree-free pixels and tree cover was overestimated in pixels with partial tree cover. Herbaceous vegetation cover was estimated with a MAE of 11.2% and a moderate prediction bias of +5.4%. The deviation of the linear model from the optimal 1:1 line reveals an overestimation of the herbaceous cover by the model for all ranges of fractional covers. Lichen, water bodies and barren surfaces were mapped with MAEs of 5.9%, 3.0% and 7.3%, respectively. However, lichen cover was below 20% in most validation pixels as higher lichen coverage at the scale of 30 × 30m is generally rare and not covered by the available VHR imagery. On average, lichen cover was moderately overestimated by 5.0%. While the model correctly identified low water coverage pixels and most fully water covered pixels, it tended to underestimate medium water factions. In pixels with <50% barren surfaces, the model tended to overestimate barren cover, while it underestimated higher barren covers.

4.2. Arctic land cover fractions across space

The multitemporal map predictions revealed distinct regional differences and environmental gradients of the land cover fractions across the greater Mackenzie Delta Region (Fig. 7 a-f; web map version at https://ows.geo.hu-berlin.de/webviewer/arctic-shrub/) See supplementary materials F for (separate) maps of shrub, coniferous, and herbaceous as well as lichen, water, and barren). To describe the spatial patterns, we refer to the most recent time period (2015–2020) in this section (Fig. 7f). Average shrub cover (including deciduous trees in the subarctic) is highest in the low Arctic tundra (47.2%), followed by the Taiga Plain (45.4%) and lowest

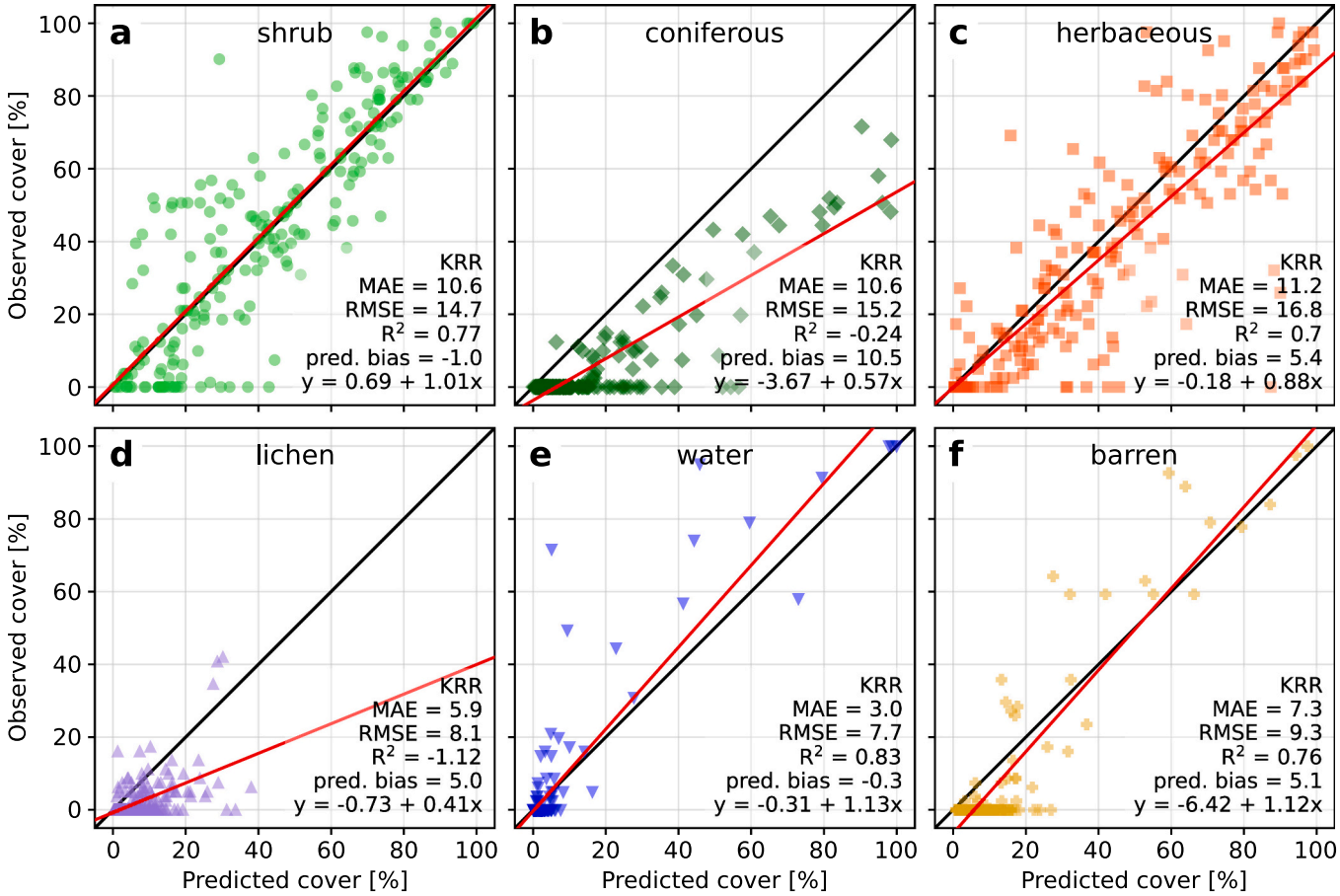

Fig. 6. Kernel Ridge Regression (KRR) ensemble prediction versus observed fractional cover of shrubs (a), coniferous trees (b), herbaceous vegetation (c), lichens (d), water (e) and barren surfaces (f).

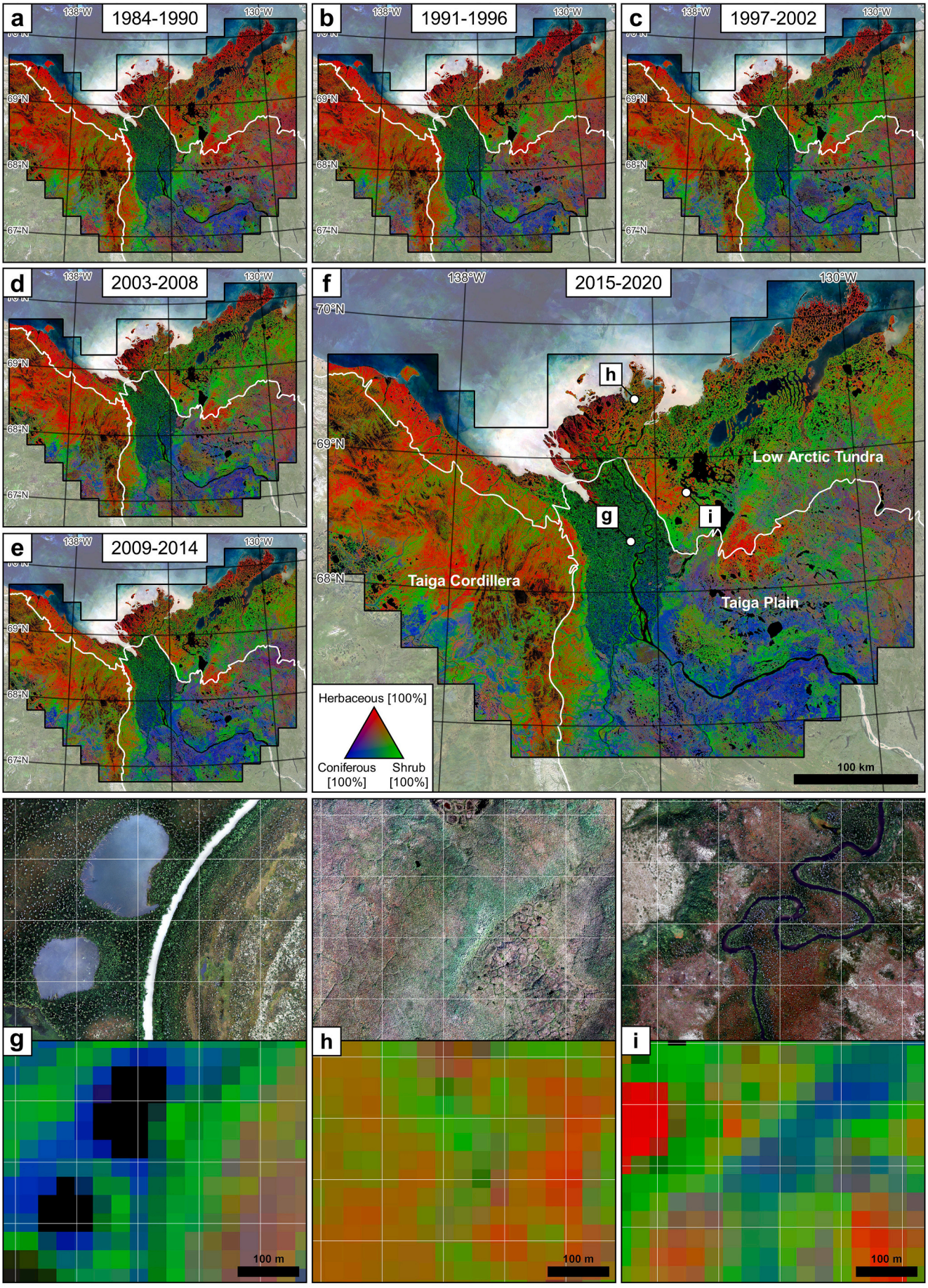

(caption on next page)

Fig. 7. Fraction cover maps of the main land surface classes shrubs, coniferous trees and herbaceous vegetation for the six observation periods (a–f) accompanied by detailed views for the recent (2015–2020) map showing a delta landscape (g) and shrub tundra (h-i). A web map version is available at https://ows.geo.hu-berlin.de/webviewer/arctic-shrub/. Single-class maps for all six cover types are provided in supplementary materials F.

in the Taiga Cordillera (37.9%) (supplementary materials F, Table F1). Coniferous trees, in contrast, have the highest cover in the south and are less frequent at higher latitudes. Strong local dominance of coniferous trees in the boreal Taiga Plains with on average 34.6% fraction cover, smoothly transitioned through the Taiga-Tundra Ecotone to reach 12.7% within the low Arctic tundra. In that regard, we emphasize the observed overestimation of coniferous tree cover of approximately +10.5% obtained from the independent accuracy assessment. Herbaceous vegetation favoured the elevated and northern regions of the study area, dominating in large parts of the lowarctic tundra (49.4%) and Taiga Cordillera (48.2%), whilst the plains of the boreal south showed a lower coverage of 30.8%. Lichen were intermixed throughout the study area with comparably stable cover across the regions (9.1–10.7%). Sub-pixel water influence (i.e., excluding masked water bodies), for instance in wetlands, covered on average 1.8–2.0%, while barren surfaces in the low-lying tundra and taiga ranged between 9.1 and 9.8% and increased in the mountainous Taiga Cordillera to 18.1%.

Besides large scale gradients, shrub cover was also related to more localized conditions. In particular in the subarctic regions, shrubs dominated on grounds previously disturbed by wildfire, often forming vast patches delineating the burn scars. Generally, previous wildfire disturbances were clearly demarcated from their surroundings by an overall increased cover of either barren, herbaceous, shrub or coniferous tree cover, depending on the relative time since fire occurrence. The dominant role of coniferous trees in the boreal parts clearly decreased with increasing latitude, forming low-density woodlands accompanied by lichens in the Taiga-Tundra Ecotone, as well as individual islands of forest stands within the otherwise shrub dominated tundra landscapes (Fig. 7i). In the delta, coniferous forest stands reached further north than in the surrounding landscapes, with single patches to entire forest stands embedded in a dense cover of shrub species (Fig. 7g). Generally, we found increased shrub abundance along streams and rivers. This included the braided river network of the low-lying Mackenzie Delta as well as creek and river valleys across the Yukon Coastal Plain. Well-drained areas with pronounced topography such as the Caribou Hills east of the alluvial plain and the foothills of the Brooks Range were characterised with an overall greater cover of herbaceous vegetation. This also applied for depressions featuring wetlands which were also almost exclusively covered by herbaceous species. Between these topographic and hydrological gradients, shrubs and herbaceous vegetation created a fine scale heterogeneous mosaic in large parts of the low Arctic landscapes, encompassing Richards Island, the lake rich coastal lowlands and large parts of the Tuktoyaktuk Peninsula (Fig. 7h).

From a methodological perspective, the overall sum of pixel-wise fraction cover components often exceeded 100%. We observed this for each observation period independently, with overall good agreement between the distributions of each time interval and the potential to mitigate this effect when correcting the estimates using the biases from the independent accuracy assessment (supplementary materials G). However, we refrained from manipulating the estimates for subsequent analyses, since a correction using the biases would treat the symptoms, not the cause. Based on visual interpretation, we found this pattern to be most strongly influenced by overpredictions of the classes coniferous and lichen. Accordingly, falsely predicted abundance of coniferous trees was identified when strong shadowing effects occurred. Furthermore, lichen, which are commonly intermixed, appeared to be additionally included in the herbaceous predictions to a large degree (Fig. 7i).

4.3. Arctic land cover fractions across time

The temporal development of land cover fractions in the Mackenzie Delta Region was characterised by net increases in shrub and coniferous tree cover, declines in herbaceous and lichen abundance and stagnating barren and water surface coverage (Fig. 8, Fig. 9). Net shrub cover increase averaged at +2.2% per decade for the entire study area. The direction and magnitude of change, however, varied across the Mackenzie Delta Region (Fig. 10a). We found opposing patterns of strong shrub increase and decline for large parts of the subarctic Taiga Plain with a net increase of +1.4% per decade. Across the Taiga Cordillera, shrub cover increased by on average + 1.6% per decade. The low Arctic tundra exhibited a net decadal increase of +4.2%, where the major hotspots of change were situated in the eastern lake-rich lowlands towards the Tuktoyaktuk Peninsula (Fig. 10a). Accordingly, the net area gained by shrub species between 1984 and 2020 was estimated at 8187 km^2, mostly attributed to net expansion between the taiga-tundra transitional zone and central low Arctic tundra (Fig. 9). However, relative to the initial shrub cover between 1984 and 1990, we found the strongest shrub cover expansion in the northernmost regions above 69.5° (Fig. 9).

Simultaneous to the extensive shrubification in the form of cover expansion, we found herbaceous and lichen cover to decline. Herbaceous vegetation decreased in all three ecoregions by decadal magnitudes of −4.3% in the low Arctic tundra, −1.2% in the Taiga Cordillera and − 2.6% in the Taiga Plains. The latitudinal pattern of herbaceous cover change largely mirrored that of shrubs in opposite direction (Fig. 9). Lichens, which were generally less abundant, decreased the strongest in the low Arctic tundra and Taiga Plain by −2.5% and − 1.8% per decade, respectively. With a net decadal increase of +1.9%, changes associated with coniferous tree cover were greatest in the southernmost boreal parts. We also found tree cover expansion to operate across the Taiga-Tundra Ecotone (Fig. 9), contributing to a net expansion of +1.0% in the Arctic tundra.

Generally, Arctic land cover fractions were not developing uniformly across the study period (Fig. 8). In the low Arctic tundra, net shrub increase was largely driven by strong expansion in earlier observational periods, while the Taiga Cordillera and Plains were characterised by rather continuous increments of smaller magnitude (Fig. 7a-f, supplementary materials H). Mapping the proportional occurrence of overall shrub cover change between the first (t_1–t_3) and second half (t_4–t_6) of the study period (Fig. 10b), we found the major hotspots of shrub proliferation during earlier timeframes to be situated in the lake-rich Tuktoyaktuk Coastlands and locally on wildfire disturbed grounds. From the lowlands towards the northernmost latitudes on the Tuktoyaktuk Peninsula, regions with a more balanced magnitude over time and greater recent expansion increased in their frequency. Similarly, the western coastal lowlands and foothills exhibited balanced and recent developments more frequently.

Local fraction cover trajectories revealed temporal developments associated with specific land surface dynamics (Fig. 11, see supplementary materials I for additional sites): This included forest gain in the subarctic characterised by gradually increasing coniferous tree cover (Fig. 11a), abrupt decline in tree cover accompanied by positive developments of barren, herbaceous and shrub cover following fire disturbance in 1999 (Fig. 11b), intensive shrubification on grounds burnt in 1968 (Fig. 11c) as well as vegetation development following lake drainage (Fig. 11d). Furthermore, other disturbances such as lake drainage, thaw slumps and river erosion affect shrub cover (supplementary materials I, Fig. I1 i-k). Undisturbed, unchanged regions were characterised by stable fraction cover trajectories with generally minor fluctuations (Fig. 11e). Along the latitudinal gradient in the Arctic tundra, we identified intense shrubification in earlier periods (Fig. 11f), uniform expansion between the entire study period (Fig. 11g), as well as relatively recent emerging shrub expansion in the northernmost regions

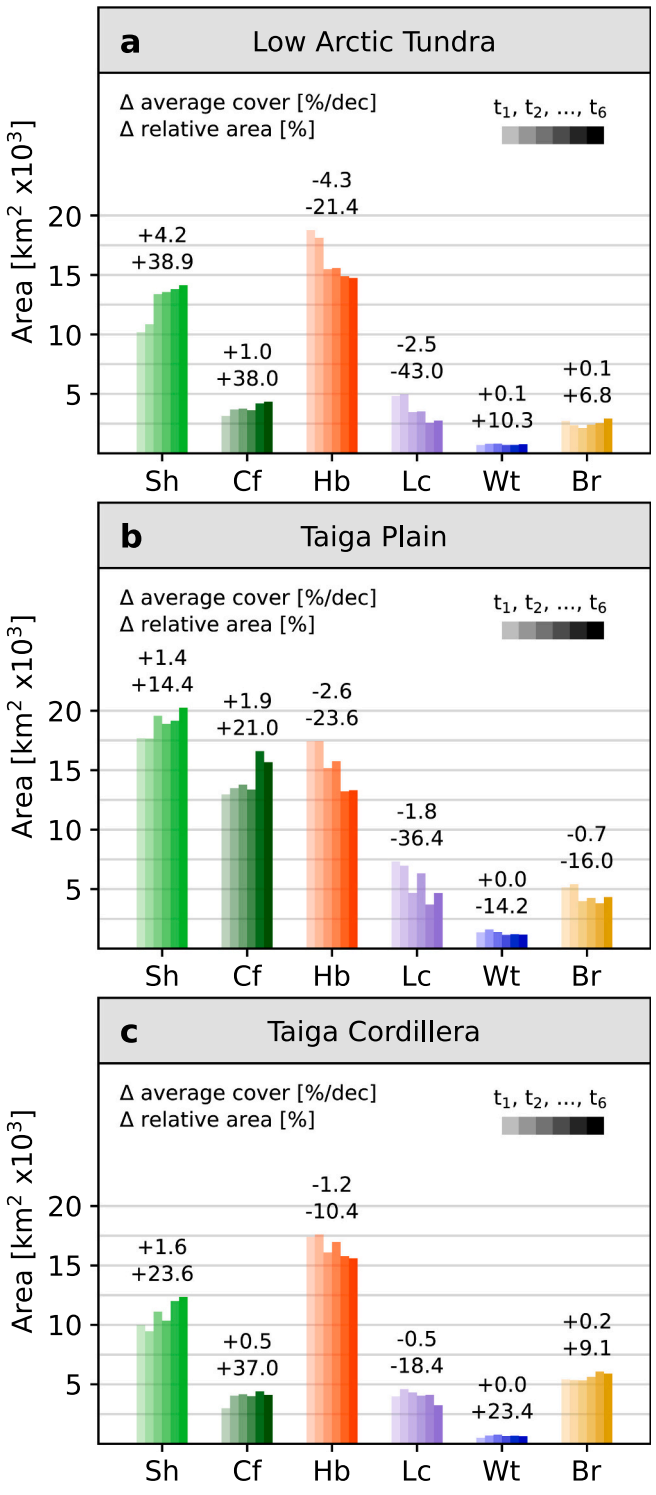

Fig. 8. Area covered by the classes shrub (Sh), coniferous (Cf), herbaceous (Hb), lichen (Lc), water (Wt), and barren (Br) for the Low Arctic Tundra (a), Taiga Plain (b), and Taiga Cordillera (c) for each observation period (t_1, t_2, …, t_6). Average pixel-wise decadal rates of change in fractional cover for each area (see Fig. 10) as well as the relative change in area covered are depicted above the bars.

(Fig. 11h), all of which associated with declines in herbaceous vegetation cover.

5. Discussion

5.1. New opportunities and persisting difficulties for Arctic fraction cover mapping

Based on the independent accuracy assessment of our mapping results, we found that the generalized multitemporal regression models are well suited for deriving fractional cover of Arctic shrub species and other land cover classes at Landsat scale. The plausibility of the approach is corroborated by the predicted spatial patterns of the land cover classes, which correspond well to expected large- and small-scale ecological gradients. However, challenges regarding Arctic fraction cover mapping and methodological limitations propagate uncertainty through the modeling process and are reflected, for instance, in varying predictive performances among target classes.

5.1.1. Arctic vegetation types in regression-based unmixing

Here, we provide the first application of regression-based unmixing using synthetically generated training data within Arctic ecosystems, mapping land cover fractions solely based on pure, temporally stable image endmember spectra. Relying upon synthetically mixed training data in biomes such as the Arctic tundra opens up new possibilities, since field data in the Arctic is scarce and not readily obtainable. However, the fine-scale structural heterogeneity of Arctic plant communities (Peterson and Billings, 1980; Epstein et al., 2004c; Lantz et al., 2010b), in combination with a target resolution of 30 m, poses challenges with regards to the identification of pure image endmembers. While some classes form distinct patterns, such as a closed-canopy shrub structure, pure endmembers of other cover types can be difficult to obtain.

We focused on mapping Arctic shrub species with a more readily identifiable closed-canopy structure, so that inter-class mixtures of non-shrub endmembers did not impact accurately regressing shrub cover. Accordingly, cover estimates of the canopy-forming shrub species were predicted with overall consistent accuracy (Macander et al., 2017). Non-vascular surface components including lichen and mosses are, however, seldomly found in pure isolation from other classes but rather form an integral part of the shrub/tussock tundra and boreal forest communities (Pearce et al., 1988). We anticipated these classes to be partly included in the herbaceous endmembers, which is perceivable in the spectral similarity of the endmember spectra and resultant net overprediction of the herbaceous fraction cover component. Similarly, coniferous tree stands vary in their growing density which - in combination with the conical shape - promotes shadowing effects and an open-canopy structure (Mcdonald et al., 1996). Based on the fact that our predictions of coniferous tree cover were systematically biased towards overestimation, we believe coniferous tree endmembers were more often influenced by background signals from other classes. Accordingly, we found areas with either pronounced topography and thus frequent shadowing, or surfaces exhibiting low reflectance due to the influence of water, as well as more open-structured woodlands to be particularly prone to overestimating coniferous tree cover. Simultaneously, intermixed, non-pure water surfaces exhibited pronounced underestimation. This was particularly evident in the northernmost coastal lowlands which had experienced substantial wetting and lake-expansion through thermoerosion (Olthof et al., 2015), leading to falsely associated (relative) increases in coniferous tree cover (Fig. 9). This inadequate separation of water, shadows and dark woody vegetation has also been reported in previous studies on fraction cover mapping (Schug et al., 2020; Suess et al., 2018). A potential correction for systematic prediction biases could encompass an intermediate accuracy assessment using an independent sample of reference data, if available. However, the final accuracy assessment of the bias corrected results would then require yet another sample of reference data to counteract overly optimistic accuracy estimates.

Although the creation of a spatially and temporally representative spectral library is not trivial (Schug et al., 2020), we emphasize that

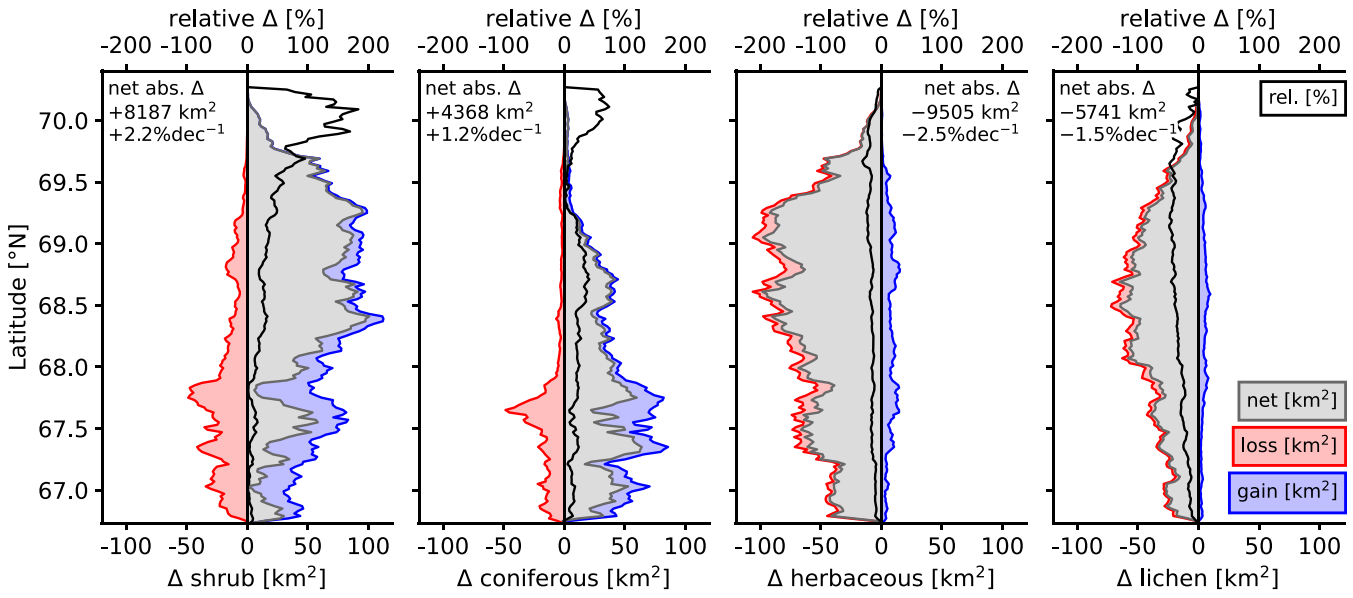

Fig. 9. Area gain (blue), loss (red) and resulting net change (grey) along the latitudinal gradient of the study area (lower x-axis) for the classes shrub, coniferous, herbaceous and lichen (summarised in 0.02° steps). The change relative to the initial class coverage is depicted in the black solid line (upper x-axis). The numbers in the upper left corner of the plot refer to the net absolute area change for the entire period and net absolute cover change per decade. (For interpretation of the references to colour in this figure legend, the reader is referred to the web version of this article.)

identifying image endmembers for Arctic land cover types at 30 m resolution allows for integrating across spectrally complex tundra vegetation types. Minor remnants of other land cover classes contained within the identified endmember pixels are a commonly accepted limitation when generating training data from synthetic mixing (Suess et al., 2018; Okujeni et al., 2021). We further emphasize that our main target class - shrubs - was not impacted by these effects, exhibiting little to no systematic over- or underestimation, and that for classes where this effect was present (e.g. coniferous), we found this effect to be consistent throughout the time series (supplementary materials G). Accordingly, relative changes in cover fractions over time might thus still be captured accurately despite class-cumulative overpredictions. Furthermore, incorporating multi-seasonal imagery might inevitably capture some degree of vertical plant structure, which could translate into the sum of the individual cover components exceeding 100%, while reference fractions derived from mono-temporal VHR imagery does not incorporate this effect. Overall, the demonstrated applicability of this approach within Arctic tundra environments is of particular interest since field data are generally scarce, often clustered regionally and temporally confined (Beamish et al., 2020), thus permitting methodological approaches that inherently rely upon adequate availability of field observations. Accordingly, previous studies had to accept limited and clustered reference data (Berner et al., 2018; He et al., 2019) or spatial and temporal mismatches between imagery and field data (Selkowitz, 2010; He et al., 2019; Macander et al., 2017). Using *synthmix*, training data can be spatially stratified across all scales to incorporate the heterogeneity of Arctic landscapes, initiating the possibility of mapping large parts of the Arctic at a high thematic detail despite insufficient field data.

Besides the complex structural component, disentangling tundra vegetation types remains difficult due to the spectral similarity of Arctic plant communities (Huemmrich et al., 2013; Bratsch et al., 2016; Beamish et al., 2017). In this study, we emulated surface component mixtures based on the assumption of linear spectral mixing. Since light interactions among surface objects can be non-linear (Borel and Gerstl, 1994; Keshava and Mustard, 2002), we expect this to impact the predictive performance of our models. However, we found our models to separate the target classes well, particularly in disentangling the heterogeneous mosaic between shrub species and herbaceous vegetation prevalent in large parts of the tundra biome. Our findings corroborate the assumption that lichens are complex to distinguish (Beamish et al., 2020), whilst canopy-forming species are regressed with greater certainty using multi-spectral imagery (Macander et al., 2017). This stems from the fact that inter-class mixtures introduce ambiguity in the spectral signal and ultimately increase the complexity of the regression task. The observed tendency of overestimating coniferous tree cover is therefore likely to be partially caused by low-growing evergreen woody vegetation, with similar spectral behaviour to coniferous trees.

As several surface types show similar spectral properties at single time points, the phenological development during the season has to be incorporated. The importance of incorporating multi-seasonal imagery for disentangling spectrally similar tundra PFTs has been stated in the context of Arctic land cover classification and fraction cover mapping (Macander et al., 2017; Karami et al., 2018; He et al., 2019; Wang et al., 2020). Particularly the value of pre- and late-seasonal information has been emphasized (Bratsch et al., 2016; Beamish et al., 2017; He et al., 2019), since woody components, herbaceous vegetation and non-vasculars exhibit different phenologies, where structural changes evoked through the senescence of vascular species expose the understory vegetation (He et al., 2019; Macander et al., 2017). In this regard, we also anticipate great potential in incorporating winter-season imagery for a better separation of coniferous trees protruding out the snow cover. However, low sun angles and ubiquitous cloud cover further decrease the already low observational density in the earlier timeframes, complicating the generation of winter-season noise- and gap-free image features across large-areas.

5.1.2. *Multi-annual and seasonal spectral-temporal-metrics*

In this work, we built upon multi-annual and seasonal STMs for deriving land cover fractions. STMs frequently form the basis for satellite-based large area mapping (Hansen et al., 2013; Venter et al., 2018; Pflugmacher et al., 2019), stemming from their ability of providing gap-free image feature across large areas and integrating across inter- and intra-class variabilities in phenology, differences in sensor properties, climate trends, and seasonal characteristics such as sun-angle variability (Suess et al., 2018). Previous work has shown the

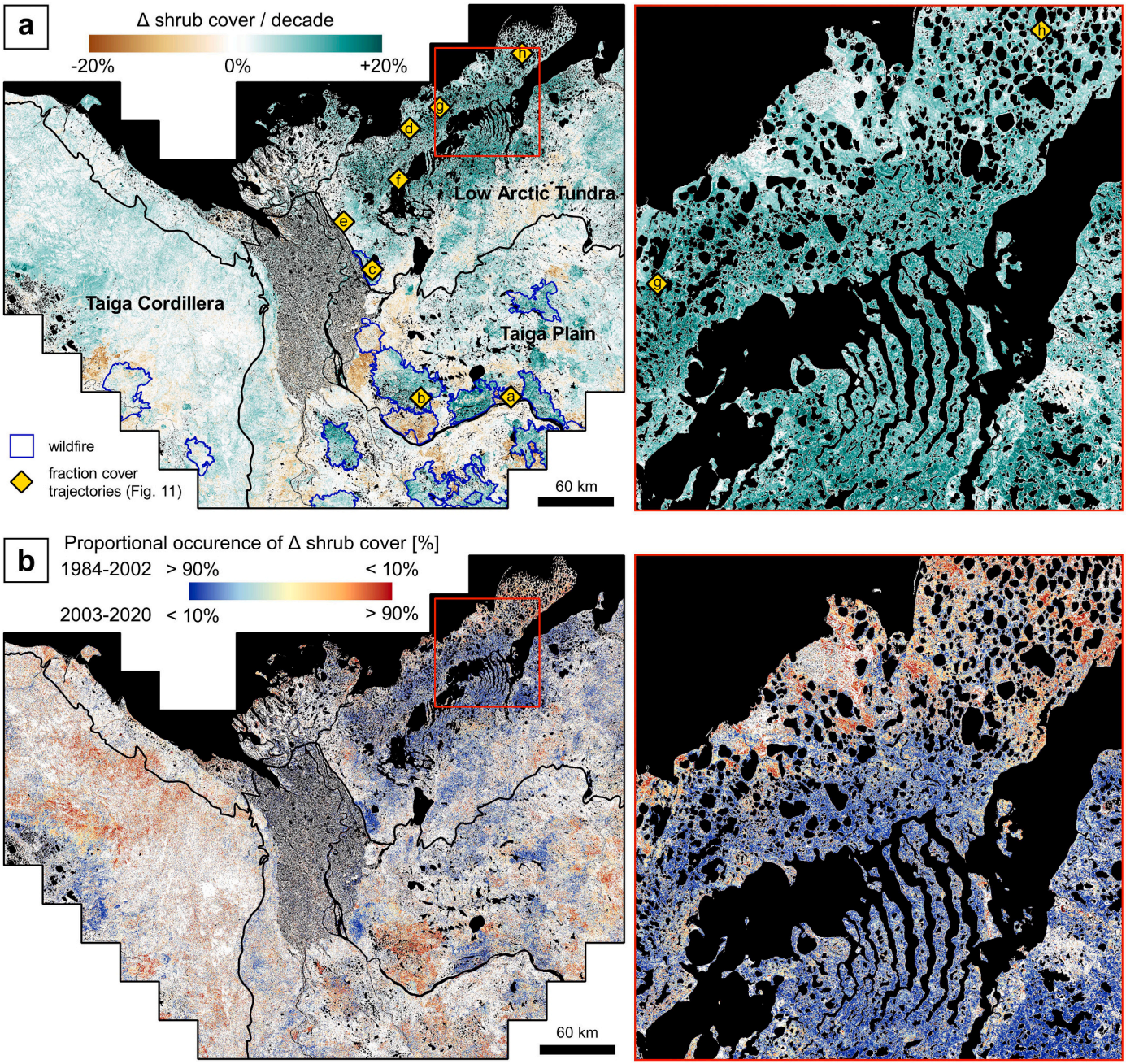

Fig. 10. Map showing the absolute decadal change in shrub cover obtained from pixel-based linear models (a), accompanied by a detailed view for parts of the Tuktoyaktuk Coastlands (web map at https://ows.geo.hu-berlin.de/webviewer/arctic-shrub/). Blue polygons in (a) depict scars of larger fires based on the National Fire Database of the Canadian Forest Service (Canadian Forest Service, 2019) and the yellow enumerated rectangles show the positions of the temporal trajectories depicted in Fig. 11. Subfigure (b) illustrates the complementary temporal occurrence of the change shown in subfigure (a), that is the proportion of the total change that occurred during each of the two periods. By comparing the magnitude of observed change during each of the two periods $t_1 - t_3$ (1984–2002) and $t_4 - t_6$ (2003–2020), the map shows if changes occurred relatively equal over time (yellow) or predominantly during the earlier (blue) or later timeframes (red). (For interpretation of the references to colour in this figure legend, the reader is referred to the web version of this article.)

applicability of STMs in quantifying fractional cover of woody features in tropical and subtropical regions (Venter et al., 2018; Higginbottom et al., 2018), for mapping urban expansion and national scale land cover (Schug et al., 2018, 2020) as well as for mapping Arctic plant communities (Macander et al., 2017). Here we corroborate the finding that regression-based unmixing using *synthmix* in combination with Landsat-derived STMs is well-suited for fraction cover mapping (Schug et al., 2020; Okujeni et al., 2021), and demonstrate the applicability of *synthmix* for disentangling fractions of shrubs and other cover types in Arctic landscapes.

Dense intra-annual image time series are needed to capture the often nuanced differences in land surface phenology between land cover types (Schwieder et al., 2016). Previous studies in Mediterranean and temperate settings made use of narrow temporal windows for the derivation of STMs or composites (Higginbottom et al., 2018; Schug et al., 2020; Okujeni et al., 2021). In Arctic contexts, however, the observational density of utilizable optical imagery is restricted by a short growing season, low sun angles and frequent cloudiness. This imposes the need for rigorous preprocessing of the imagery and potentially integrating across seasonal imagery from multiple years in order to

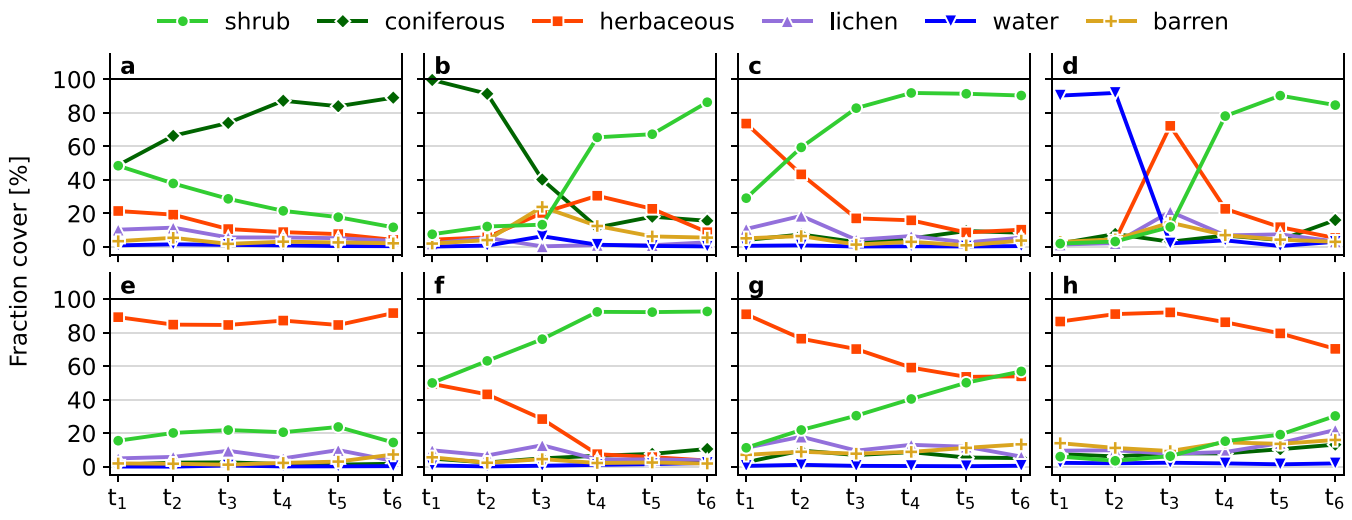

Fig. 11. Fraction cover trajectories for selected sites whose locations are depicted in Fig. 10a. The trajectories comprise subarctic forest gain (a), subarctic vegetation succession following wildfire disturbance in 1999 (b), intense tundra shrubification on grounds burnt in 1968 (c), thermokarst lake drainage (d), unchanged surfaces (e), as well as gradual shrub expansion along a latitudinal gradient with change during the earlier (f), the entire (g) and the later (h) observational periods.

guarantee a spatio-temporal consistent quality of input features (Selkowitz, 2010). Accordingly, previous work on deriving monotemporal fractional cover in tundra landscapes relied upon integrating several years (5–16 years) of imagery for creating image composites or STMs (He et al., 2019; Macander et al., 2017). Here, we collapsed the study period from 1984 to 2020 into six distinct epochs, each comprising 6 years (7 years for 1984–1990) of image acquisitions. In combination with rigorous preprocessing of the Landsat imagery, fusing the observations from each 6-year epoch into an artificial single year resulted in a dense time series representing the intra-annual phenology of the pixels. Smoothing this dense time series using RBF-kernel based interpolation allowed for deriving virtually noise-free, high-quality STMs within comparably narrow windows of time. This is particularly important for the earlier epochs only covered by Landsat-5 with less frequent image acquisitions. Yet aggregating the time series into six epochs was not only necessary due to data availability and image quality concerns, but also reasonable, given that our main goal was to quantify gradual shrub cover dynamics over multiple decades. A similar temporal aggregation approach has been applied for mapping woody plant encroachment in Africa (Venter et al., 2018). However, restricting the temporal resolution to 6-year epochs implies that abrupt land surface change triggered by disturbance events is smoothed. If such fine temporal scales are required, fusing observations from Landsat and Sentinel-2 holds great potential for future adaptions of the approach, though this will inevitably be limited to recent years (2015-).

5.1.3. *Global multitemporal regression models*

We specifically targeted the applicability of our models across time by building single, class-wise, multitemporal regression models, instead of modeling each time period separately. Thereby, inter- and intra-class variabilities owing to phenology, differences in sensor properties, climate trends, and seasonal characteristics become integrated across the entire study period, reducing the impact of systematic and random errors within single observational years and enabling the comparability of fractions across time (Suess et al., 2018). Compared to modeling each time period separately using models trained solely on data from the respective time steps, multitemporal modeling likely increases the complexity of the regression problem, since integrating across the aforementioned factors implies including greater variance in the data. However, it is a trade-off between maximising single time period prediction accuracy and multitemporal applicability of the models. Since field observations or suitable VHR imagery are only available for the 2015–2020 period, we utilised the independent assessment of the recent fraction cover predictions as surrogate for the expected overall accuracy of the models. We thus acknowledge that some degree of prediction uncertainty across the time series remains elusive. However, we emphasize the overall good predictive model performance on the recent, independently validated period, while the STM features the models were trained on are derived from >80% of 1984–2014 imagery (since each of the six periods on averages contributes 1/6 of STM in the random synthetic data generation process). Furthermore, Senf et al. (2020) found the largest impact on prediction uncertainty to predominately originate from deviances in the date of image acquisition using best-available-pixel composites. Here, we specifically counteract the influence of single observations and resultant single year fluctuations in the time series by using STMs derived from dense, multi-annually aggregated image time series. Accordingly, multi-decadal change originating from abrupt and gradual processes can be tracked in an environment with a short seasonal window and low intra-annual acquisition density, while the temporal trajectories exhibit marginal fluctuations (Fig. 11). Our results corroborate the suitability of multitemporal regression modeling for fraction cover mapping beyond Mediterranean shrub cover (Suess et al., 2018), urban development (Schug et al., 2018) or forest cover types (Senf et al., 2020).

In summary, our results demonstrate the applicability of using Landsat image features and regression-based unmixing of synthetic training data to estimate fractional cover of Arctic shrubs and other land cover types. Our approach differs from previous mapping exercises in the Arctic context which either relied upon field observations (Selkowitz, 2010; Macander et al., 2017; He et al., 2019) or VHR imagery derived training data (Olthof and Fraser, 2007; Beck et al., 2011), yet we retrieved shrub cover at comparable good accuracy (RMSE of 14.7% here versus 9.4–19.0%). However, the comparability of predictive capabilities among studies suffers from differences in the validation strategy (e.g. fully independent; left-out samples of clustered data), class definitions and field data availability. Accordingly, He et al. (2019) found substantial discrepancies in estimated fractional cover when comparing their model predictions to Macander et al. (2017) and Beck et al. (2011) in Arctic Alaska. In this regard, our method may contribute to the need for more unifying and comparable approaches when aiming at assessing spatial and temporal developments across different regions of the Arctic. Ultimately, the applicability of our approach for Arctic landscapes will be conditioned to a large degree by the sufficient availability of satellite observations, with substantial discrepancies existing within the northern latitudes (Zhu et al., 2019).

5.2. Arctic fractional cover across space and time

5.2.1. Tundra vegetation mosaics of the Mackenzie Delta region mapped

We found the map predictions to agree well with expected large-scale climatic environmental gradients driven by latitude, topography and coastal proximity. The latitudinal decrease of coniferous tree cover outlines the trajectory from dense forest cover in the subarctic, that transitions into open-canopy forests and woodlands, to finally isolated patches of tree stands in the northern sections of the Taiga-Tundra Ecotone (Timoney et al., 1992). In parallel, shrubs and herbaceous vegetation increase in their dominance, characterising the transition of subarctic boreal forests to shrub tundra landscapes (Burn and Kokelj, 2009; Lantz et al., 2010b). Further north, the complex vegetation mosaic of the shrub-tundra becomes increasingly dominated by herbaceous species such as tussock-forming sedges (Lantz et al., 2010b), expressed in parallel by the gradual decline of shrub cover on the coastal lowlands and the northern Tuktoyaktuk Peninsula. Lichens largely mirror the pattern of coniferous tree cover, which agrees with the presence of open lichen woodlands in large parts of the subarctic regions (Pearce et al., 1988) as well as lichen-rocklands found on outcrops east of the delta (Timoney et al., 1992).

On a finer scale, the fraction maps are able to delineate the local dominance of PFTs associated with specific landscape settings as well as the heterogeneous mosaic of plant communities, driven by landscape microtopography and disturbance history (Peterson and Billings, 1980). Accordingly, we found shrubs to be increasingly located on grounds with generally good nutrient availability and moist, non-waterlogged conditions, as found in riparian settings (Grünberg et al., 2020; Liljedahl et al., 2020), along hillslopes (Tape et al., 2006), and following wildfire disturbance (Landhausser and Wein, 1993; Lantz et al., 2010a; Gaglioti et al., 2021). Herbaceous vegetation, in contrast, prevailed in sedge dominated wetlands along the coastal lowlands and river estuaries and on grass-dominated hilltops (Burn and Kokelj, 2009).

This study extents the mapping of the Mackenzie Delta Region beyond categorical land cover (Bartsch et al., 2019; Wang et al., 2020), providing a comprehensive portrayal of the large scale gradients and the fine-scale heterogeneous nature of Arctic vegetation types in the Mackenzie Delta Region. It enables incorporating a more accurate representation of land surface conditions when modeling land-atmosphere interactions (Loranty et al., 2011; Muster et al., 2012) or assessing vegetation-permafrost dynamics (Heijmans et al., 2022).

5.2.2. Shrub cover expansion revealed

The results suggest widespread occurrence of expanding shrub cover, averaging at +2.2% per decade for the entire study area and + 4.2% per decade for the low Arctic tundra. Net area gained by shrub species was largest within the Taiga-Tundra transitional zone and southern low Arctic tundra while relative shrub expansion was strongest in the northernmost regions (>69.5°N). From a broad-scale perspective, this corroborates evidence of widespread shrub expansion in the greater Mackenzie Delta Region (Lantz et al., 2013; Fraser et al., 2014a; Myers-Smith et al., 2019). Generally, shrubification has been linked to warming air temperatures, owing to the climate sensitivity of many shrub species (Myers-Smith et al., 2015b). Accordingly, continuously increasing air temperatures of >2.5 °C in the central Mackenzie Delta Region since 1970 (Burn and Kokelj, 2009), corroborates the attribution of warming as major underlying causal mechanism behind large scale shrubification in the study area (Fraser et al., 2014a).

Our estimates of area-wide magnitude of shrub cover change are closely related to local evidence of shrub encroachment, acknowledging differences in the observed physiognomy (e.g. tall shrubs only), spatial scale and temporal timeframes observed. First, this encompasses regions outside the Western Canadian Arctic, including northern Québec (+4.2% dec^{-1} 1957–2008, Ropars and Boudreau, 2012), northern Alaska (+1.0–1.6% dec^{-1} tall shrubs 1950s–2000s, Tape et al., 2006) and longitudinal gradients of northern Siberia (+1.3–6.0% dec^{-1} 1960s–2000s, Frost and Epstein, 2014). Second, the expansion rates derived here in the low Arctic tundra correspond well to local evidence of shrub encroachment within the Mackenzie Delta Region, with decadal increases in average shrub cover of +4.5% in the upland tundra north of Inuvik between 1972 and 2004 (Lantz et al., 2013), as well as +5.9% (Fraser et al., 2014a) and + 2.3–3.5% (Moffat et al., 2016) on the Tuktoyaktuk Coastlands between 1980 and 2013. We mapped the spatio-temporal dynamics of this process at 30 m pixel resolution for an area of 143,100 km^2, thus extending the spatial dimensions at which shrub encroachment can be directly quantified.

Our results show that the dynamics of shrub expansion in this region have not been uniform across space and time, suggesting that shrubification is modified by several interacting site-specific factors, including soil moisture regime, topography, herbivory intensity, and disturbance (Myers-Smith et al., 2015b; Martin et al., 2017; Mekonnen et al., 2021). Such local-scale heterogeneity in changing vegetation productivity has also been described in the Mackenzie Delta region (Seider et al., 2022). Our fraction maps depict clear signs of accelerated and intensive shrub increase on grounds previously disturbed by wildfire (Canadian Forest Service, 2019). In the subarctic, we found fraction cover trajectories to match the expected stages of secondary succession of boreal forests (Fig. 11a-b), initiated by burned barren ground developing into a mosaic of herbaceous and shrubby vegetation, followed by mostly deciduous shrub/tree dominance and the regrowth of coniferous trees (Viereck et al., 1981). Generally, the largest changes in coniferous tree cover were found in the southern boreal plains. While evergreen forest gains occur within the subarctic regions of north-western Canada (Wang et al., 2020), the actual forest extent appears to be stationary in the region (Rees et al., 2020). Given the prediction accuracy of coniferous tree cover, the magnitude of change observed and the spectral similarity to other surface types, we thus anticipate that the observed coniferous tree gains are to some extent also reflecting increases in shrub cover and wetting processes, especially within the low Arctic tundra. In the tundra and the Taiga-Tundra transitional zone we observed a development towards dense shrub cover, matching the observed succession of tall deciduous shrub and tree species in that region (Landhausser and Wein, 1993; Lantz et al., 2010a). Generally, fire events have shown to accelerate ecological processes, including shrub expansion, which in the absence of fire disturbance exhibit a rather lagged response to increasing temperatures (Gaglioti et al., 2021). There is observational evidence that shrub expansion, concomitant with greater fuel load, can trigger positive feedback of increased fire frequency and magnitude. Under continued warming, this process is expected to move northwards and accelerate the latitudinal expansion of tall shrub species into dwarf-shrub and tussock tundra (Gaglioti et al., 2021).

Our results suggest that shrub expansion was often accompanied by declining herbaceous vegetation and lichen cover. Generally, tundra shrubification is largely enabled by the competitive advantage of deciduous species over other PFTs in a warming environment (Chapin et al., 1996; Myers-Smith et al., 2011). Shrubs have shown to take advantage of increased nutrient availability (Bret-Harte et al., 2002; Chapin et al., 1996) and their relatively taller growth form entails a reduced interception of light for low-growing species in the understory (Epstein et al., 2004a; Mekonnen et al., 2018). Long-term monitoring and experimental studies therefore suggest that shrubification mostly occurs at the expense of evergreen shrubs and non-vascular lichen and mosses, with evidence that herbaceous graminoids are gaining biomass in conjunction with deciduous shrub species (Epstein et al., 2004a; Myers-Smith et al., 2019). In their pan-Arctic review, Elmendorf et al. (2012) found positive trends of graminoid cover in colder sites and neutral to negative trends at warmer sites, suggesting strong regional variability of vegetation development in response to continued warming. Experimental projections expect progressing homogenisation of Arctic plant communities (Stewart et al., 2018), characterised by a decrease of non-vasculars and graminoids in an increasingly shrub dominated landscape, while graminoids and non-vasculars will gain

biomass in the colder high Arctic regions (Mekonnen et al., 2018). Given the comparably warm, moist conditions within the low Arctic tundra landscapes of the Mackenzie Delta Region, shrub encroachment could well be occurring at the expense of graminoid and lichen cover. Fraser et al. (2014a) found increased canopy cover of erect dwarf and tall shrubs to be accompanied by lichen decline. On the Tuktoyaktuk Coastal Plain, Moffat et al. (2016) report plot-based evidence that average sedge cover decreased by 0.5–2.3% per decade and and lichen cover decreased by 0.5–3.1% per decade. Generally, these rates are in a similar order of magnitude with the −4.3% in herbaceous and − 2.5% in lichen cover we observed. The yet apparent discrepancies corroborate our assumption that lichen spectra are captured within the herbaceous endmembers, potentially overestimating herbaceous decline. Furthermore, a top-of-canopy approach is inherently limited in capturing the vertical structure of vegetation and thus largely neglects understory plant communities.

Extensive shrub expansion predominantly occurred in the taiga-tundra transitional zone and along the lake-rich coastal lowlands of the tundra, including the Tuktoyaktuk Coastlands and Richards Island. From a temporal perspective, we found shrub encroachment within these regions to have predominately occurred in the earlier periods (t_1–t_3, 1984–2002), developing towards rather stable shrub cover trajectories in recent decades. First, this matches the expectation that vegetation responses to warming will onset the strongest at the transition between shrub and tussock tundra (Epstein et al., 2004b). Second, this is in line with the conception that shrub expansion is largely influenced by the prevalent moisture regime (Myers-Smith et al., 2015a), generally favouring wetter over drier regions of the tundra (Tape et al., 2006; García Criado et al., 2020; Liljedahl et al., 2020). The landscapes east of the delta, with their rolling hills and low-lying depressions featuring thermokarst lakes are thus highly suitable of facilitating intense shrubification. Similarly, the riparian zones at the foothills along the Yukon Coastal Plain in the west depict amplified signs of shrub encroachment. In the northernmost areas of the Tuktoyaktuk Peninsula and western coastal plains, the maps either depict a rather continuous shrub cover development (Fig. 11g) or more recent onset of shrub encroachment (Fig. 11h). Additionally, relative shrub expansion was strongest in the northernmost regions (>69.5°N). Overall, this may suggest that potentially two mechanisms of shrubification have been operating in the Mackenzie Delta Region: (1) the lateral growth and recruitment between existing patches in an already shrub dominated landscape and (2) the range expansion of shrubs into formerly low-statured tundra communities (Myers-Smith et al., 2011). Although a gradual latitudinal expansion appears coherent with the climate sensitivity of shrub growth, and further corroborates projected advancements of shrub species under changing climatic gradients (Epstein et al., 2004a), evidence for Arctic latitudinal shrubline advance is currently insufficient (Myers-Smith and Hik, 2018). Following thorough calibration to field-based evidence in Alpine regions where shrubline advance has been explicitly studied (Myers-Smith and Hik, 2018), our method could help illuminating our understanding of northwards directed shrub proliferation.

6. Conclusion

In this study, we assessed the suitability of regression-based unmixing using synthetic training data for disentangling the fine-scale heterogeneous mosaic and temporal development of Arctic vegetation types. We illustrate the potential in deriving fractional cover of various surface types at a high level of detail using machine learning in combination with multi-temporal synthetic training data and Landsat-based image features. Despite a wide array of persisting complexities and uncertainties, our approach creates new opportunities for mapping the vast and remote landscapes of the Arctic tundra independent of sparsely existent field observations. Multitemporal, vegetation-type specific fraction cover estimates enable a more accurate and more adequate representation of surface composition and structure than time series of non-distinctive spectral indices or discrete classifications. Our fraction cover estimates address the still existing gap between high-quality field observations and large-scale assessments of ecological change. The multitemporal regression models corroborate findings of extensive shrub expansion in the Mackenzie Delta Region of the Western Canadian Arctic, while capturing the heterogeneity of this process at a high level of detail. The maps thus provide a new basis for a spatially explicit assessment of the underlying mechanisms and their site-specific interactions of shrub expansion. Deploying the method in other regions with existing field observations has the potential to further consolidate our understanding of the method's applicability across other parts of the tundra biome. Sensor-fusion between Landsat and Sentinel-2 holds potential for future adaptions of the approach, including deriving denser fraction cover time series for the more recent change history. Generally, uniform and scalable mapping techniques of this kind complement high-quality field work and are needed to disentangle key ecosystem-level processes, including shrubline advance, on the pan-Arctic scale.

CRediT authorship contribution statement

Leon Nill: Conceptualization, Methodology, Software, Validation, Investigation, Writing – original draft, Visualization, Writing – review & editing. **Inge Grünberg:** Validation, Resources, Investigation, Writing – review & editing. **Tobias Ullmann:** Validation, Investigation, Writing – review & editing, Funding acquisition. **Matthias Gessner:** Resources, Writing – review & editing. **Julia Boike:** Supervision, Resources, Writing – review & editing, Funding acquisition. **Patrick Hostert:** Supervision, Resources, Writing – review & editing, Funding acquisition.

Declaration of Competing Interest

The authors declare that they have no known competing financial interests or personal relationships that could have appeared to influence the work reported in this paper.

Data availability

Data will be made available on request.

Acknowledgements

This research contributes to the Global Land Programme (https://glp.earth/) and to the Landsat Science Team 2018-2023 (https://www.usgs.gov/core-science-systems/nli/landsat/landsat-science-teams). Inge Grünberg was funded by Helmholtz Imaging, a platform of the Helmholtz Incubator on Information and Data Science [grant number: ZT-I-PF-4-001]. Field work was funded by the German Research Foundation (DFG) [grant number: 329721376]. We thank three anonymous reviewers for contributing constructive feedback and suggestions to the manuscript.

Appendix A. Supplementary data

Supplementary data to this article can be found online at https://doi.org/10.1016/j.rse.2022.113228.

References

Andreu-Hayles, L., Gaglioti, B.V., Berner, L.T., Levesque, M., Anchukaitis, K.J., Goetz, S. J., D'Arrigo, R., 2020. A narrow window of summer temperatures associated with shrub growth in Arctic Alaska. Environ. Res. Lett. 15 https://doi.org/10.1088/1748-9326/ab897f.

Bartsch, A., Hofler, A., Kroisleitner, C., Trofaier, A.M., 2016. Land cover mapping in northern high latitude permafrost regions with satellite data: achievements and remaining challenges. Remote Sens. 8, 1–27. https://doi.org/10.3390/rs8120979.

Bartsch, A., Widhalm, B., Pointner, G., Ermokhina, K., Leibman, M., Heim, B., 2019. Landcover derived from Sentinel-1 and Sentinel-2 satellite data (2015-2018) for subarctic and arctic environments. https://doi.org/10.1594/PANGAEA.897916.

Baumann, M., Levers, C., Macchi, L., Bluhm, H., Waske, B., Gasparri, N.I., Kuemmerle, T., 2018. Mapping continuous fields of tree and shrub cover across the Gran Chaco using Landsat 8 and Sentinel-1 data. Remote Sens. Environ. 216, 201–211. https://doi.org/10.1016/j.rse.2018.06.044.

Beamish, A., Coops, N., Chabrillat, S., Heim, B., 2017. A phenological approach to spectral differentiation of low-Arctic Tundra vegetation communities, north slope, Alaska. Remote Sensing 9, 1200. https://doi.org/10.3390/rs9111200.

Beamish, A., Raynolds, M.K., Epstein, H., Frost, G.V., Macander, M.J., Bergstedt, H., Bartsch, A., Kruse, S., Miles, V., Tanis, C.M., Heim, B., Fuchs, M., Chabrillat, S., Shevtsova, I., Verdonen, M., Wagner, J., 2020. Recent trends and remaining challenges for optical remote sensing of Arctic tundra vegetation: a review and outlook. Remote Sens. Environ. 246, 111872 https://doi.org/10.1016/j.rse.2020.111872.

Beck, P.S.A., Goetz, S.J., 2011. Satellite observations of high northern latitude vegetation productivity changes between 1982 and 2008: ecological variability and regional differences. Environ. Res. Lett. 6, 45501. https://doi.org/10.1088/1748-9326/6/4/045501.

Beck, P., Horning, N., Goetz, S., Loranty, M., Tape, K., 2011. Shrub cover on the north slope of Alaska: a circa 2000 baseline map. Arct. Antarct. Alp. Res. 43, 355–363. https://doi.org/10.1657/1938-4246-43.3.355.

Bergstra, J., Bardenet, R., Bengio, Y., Kégl, B., 2011. Algorithms for hyper-parameter optimization. In: Shawe-Taylor, J., Zemel, R., Bartlett, P., Pereira, F., Weinberger, K. Q. (Eds.), Advances in Neural Information Processing Systems. Curran Associates, Inc., pp. 1–9. In: https://proceedings.neurips.cc/paper/2011/file/86e8f7ab32cfd12577bc2619bc635690-Paper.pdf

Berner, L.T., Jantz, P., Tape, K.D., Goetz, S.J., 2018. Tundra plant above-ground biomass and shrub dominance mapped across the north slope of Alaska. Environ. Res. Lett. 13 https://doi.org/10.1088/1748-9326/aaaa9a.

Berner, L.T., Massey, R., Jantz, P., Forbes, B.C., Macias-Fauria, M., Myers-Smith, I., Kumpula, T., Gauthier, G., Andreu-Hayles, L., Gaglioti, B.V., Burns, P., Zetterberg, P., D'Arrigo, R., Goetz, S.J., 2020. Summer warming explains widespread but not uniform greening in the Arctic tundra biome. Nat. Commun. 11, 1–12. https://doi.org/10.1038/s41467-020-18479-5.

Biskaborn, B.K., Smith, S.L., Noetzli, J., Matthes, H., Vieira, G., Streletskiy, D.A., Schoeneich, P., Romanovsky, V.E., Lewkowicz, A.G., Abramov, A., Allard, M., Boike, J., Cable, W.L., Christiansen, H.H., Delaloye, R., Diekmann, B., Drozdov, D., Etzelmüller, B., Grosse, G., Guglielmin, M., Ingeman-Nielsen, T., Isaksen, K., Ishikawa, M., Johansson, M., Johannsson, H., Joo, A., Kaverin, D., Kholodov, A., Konstantinov, P., Kröger, T., Lambiel, C., Lanckman, J.P., Luo, D., Malkova, G., Meiklejohn, I., Moskalenko, N., Oliva, M., Phillips, M., Ramos, M., Sannel, A.B.K., Sergeev, D., Seybold, C., Skryabin, P., Vasiliev, A., Wu, Q., Yoshikawa, K., Zheleznyak, M., Lantuit, H., 2019. Permafrost is warming at a global scale. Nat. Commun. 10, 1–11. https://doi.org/10.1038/s41467-018-08240-4.

Bjorkman, A.D., García Criado, M., Myers-Smith, I.H., Ravolainen, V., Jónsdóttir, I.S., Westergaard, K.B., Lawler, J.P., Aronsson, M., Bennett, B., Gardfjell, H., Heiðmarsson, S., Stewart, L., Normand, S., 2020. Status and trends in Arctic vegetation: evidence from experimental warming and long-term monitoring. Ambio 49, 678–692. https://doi.org/10.1007/s13280-019-01161-6.

Bonney, M.T., Danby, R.K., Treitz, P.M., 2018. Landscape variability of vegetation change across the forest to tundra transition of Central Canada. Remote Sens. Environ. 217, 18–29. https://doi.org/10.1016/j.rse.2018.08.002.

Borel, C.C., Gerstl, S.A., 1994. Nonlinear Spectral Mixing Models for Vegetative and Soil Surfaces. Technical Report..

Bratsch, S.N., Epstein, H.E., Buchhorn, M., Walker, D.A., 2016. Differentiating among four Arctic tundra plant communities at ivotuk,Alaska using field spectroscopy. Remote Sensing 8. https://doi.org/10.3390/rs8010051.

Bret-Harte, M.S., Shaver, G.R., Chapin, F.S., 2002. Primary and secondary stem growth in arctic shrubs: implications for community response to environmental change. J. Ecol. 90, 251–267. https://doi.org/10.1046/j.1365-2745.2001.00657.x.

Burn, C.R., Kokelj, S.V., 2009. The environment and permafrost of the Mackenzie Delta area. Permafrost and Periglacial Processes 20, 83–105. https://doi.org/10.1002/ppp.655.

Canadian Forest Service, 2019. National Fire Database – Agency Fire Data. Natural Resources Canada. Canadian Forest Service, Northern Forestry Centre. http://cwfis.cfs.nrcan.gc.ca/ha/nfdb.

Chang, C.I., Plaza, A., 2006. A fast iterative algorithm for implementation of pixel purity index. IEEE Geosci. Remote Sens. Lett. 3, 63–67. https://doi.org/10.1109/LGRS.2005.856701.

Chapin, F.S., Bret-Harte, M.S., Hobbie, S.E., Zhong, H., 1996. Plant functional types as predictors of transient responses of arctic vegetation to global change. J. Veg. Sci. 7, 347–358. https://doi.org/10.2307/3236278.

Cooper, S., Okujeni, A., Jänicke, C., Clark, M., van der Linden, S., Hostert, P., 2020. Disentangling fractional vegetation cover: Regression-based unmixing of simulated spaceborne imaging spectroscopy data. Remote Sens. Environ. 246, 111856 https://doi.org/10.1016/j.rse.2020.111856. https://linkinghub.elsevier.com/retrieve/pii/S0034425720302261.

Crist, E.P., 1985. A TM tasseled cap equivalent transformation for reflectance factor data. Remote Sens. Environ. 17, 301–306. https://doi.org/10.1016/0034-4257(85)90102-6.

Ecological Stratification Working Group, 1996. A National Ecological Framework for Canada. Technical Report. Agriculture and Agri-Food Canada, Research Branch, Centre for Land and Biological Resources Research, and Environment Canada, State of the Environment Directorate, Ecozone Analysis Branch. Ottawa/Hull.

Elmendorf, S.C., Henry, G.H., Hollister, R.D., Björk, R.G., Bjorkman, A.D., Callaghan, T. V., Collier, L.S., Cooper, E.J., Cornelissen, J.H., Day, T.A., Fosaa, A.M., Gould, W.A., Grétarsdóttir, J., Harte, J., Hermanutz, L., Hik, D.S., Hofgaard, A., Jarrad, F., Jónsdóttir, I.S., Keuper, F., Klanderud, K., Klein, J.A., Koh, S., Kudo, G., Lang, S.I., Loewen, V., May, J.L., Mercado, J., Michelsen, A., Molau, U., Myers-Smith, I.H., Oberbauer, S.F., Pieper, S., Post, E., Rixen, C., Robinson, C.H., Schmidt, N.M., Shaver, G.R., Stenström, A., Tolvanen, A., Totland, O., Troxler, T., Wahren, C.H., Webber, P.J., Welker, J.M., Wookey, P.A., 2012. Global assessment of experimental climate warming on tundra vegetation: heterogeneity over space and time. Ecol. Lett. 15, 164–175. https://doi.org/10.1111/j.1461-0248.2011.01716.x.

Environment Canada, 2021. 1981-2010 Climate Normals & Averages. https://climate.weather.gc.ca/climate_normals/index_e.html.

Epstein, H.E., Beringer, J., Gould, W.A., Lloyd, A.H., Thompson, C.D., Chapin, F.S., Michaelson, G.J., Ping, C.L., Rupp, T.S., Walker, D.A., 2004a. The nature of spatial transitions in the Arctic. J. Biogeogr. 31, 1917–1933. https://doi.org/10.1111/j.1365-2699.2004.01140.x.

Epstein, H.E., Beringer, J., Gould, W.A., Lloyd, A.H., Thompson, C.D., Chapin, F.S., Michaelson, G.J., Ping, C.L., Rupp, T.S., Walker, D.A., 2004b. The nature of spatial transitions in the Arctic. J. Biogeogr. 31, 1917–1933. https://doi.org/10.1111/j.1365-2699.2004.01140.x.

Epstein, H.E., Calef, M., Walker, M., Energy, H., 2004. Detecting changes in arctic tundra plant communities in response to warming over decadal time scales Aeolian processes and ecosystem change in southern New Mexico View project Permafrost Arctic Research using remote sensing and Deep Learning Neural Networks View project. Article in Global Change Biology. https://doi.org/10.1111/j.1365-2486.2004.00810.x. https://www.researchgate.net/publication/297534472.

Frantz, D., 2019. FORCE-landsat + Sentinel-2 analysis ready data and beyond. Remote Sens. 11 https://doi.org/10.3390/rs11091124.

Frantz, D., Roder, A., Stellmes, M., Hill, J., 2016. An operational radiometric Landsat preprocessing framework for large-area time series applications. IEEE Trans. Geosci. Remote Sens. 54, 3928–3943. https://doi.org/10.1109/TGRS.2016.2530856. http://ieeexplore.ieee.org/document/7426833/.

Frantz, D., Stellmes, M., Hostert, P., 2019. A global MODIS water vapor database for the operational atmospheric correction of historic and recent landsat imagery. Remote Sens. 11 https://doi.org/10.3390/rs11030257.

Fraser, R.H., Olthof, I., Carrière, M., Deschamps, A., Pouliot, D., 2011. Detecting long-term changes to vegetation in northern Canada using the Landsat satellite image archive. Environ. Res. Lett. 6 https://doi.org/10.1088/1748-9326/6/4/045502.

Fraser, R.H., Lantz, T.C., Olthof, I., Kokelj, S.V., Sims, R.A., 2014a. Warming-induced shrub expansion and lichen decline in the Western Canadian Arctic. Ecosystems 17, 1151–1168. https://doi.org/10.1007/s10021-014-9783-3.

Fraser, R.H., Olthof, I., Kokelj, S.V., Lantz, T.C., Lacelle, D., Brooker, A., Wolfe, S., Schwarz, S., 2014b. Detecting landscape changes in high latitude environments using landsat trend analysis: 1. Visualization. Remote Sens. 6, 11533–11557. https://doi.org/10.3390/rs61111533.

Frost, G.V., Epstein, H.E., 2014. Tall shrub and tree expansion in siberian tundra ecotones since the 1960s. Glob. Chang. Biol. 20, 1264–1277. https://doi.org/10.1111/gcb.12406.

Frost, G.V., Epstein, H.E., Walker, D.A., 2014. Regional and landscape-scale variability of Landsat-observed vegetation dynamics in northwest Siberian tundra. Environ. Res. Lett. 9 https://doi.org/10.1088/1748-9326/9/2/025004.

Gaglioti, B.V., Berner, L.T., Jones, B.M., Orndahl, K.M., Williams, A.P., Andreu-Hayles, L., D'Arrigo, R.D., Goetz, S.J., Mann, D.H., 2021. Tussocks enduring or shrubs greening: alternate responses to changing fire regimes in the Noatak River valley,Alaska. Journal of Geophysical Research: Biogeosciences 126. https://doi.org/10.1029/2020jg006009.

Gao, B.C., 1996. NDWI—A normalized difference water index for remote sensing of vegetation liquid water from space. Remote Sens. Environ. 58, 257–266. https://doi.org/10.1016/S0034-4257(96)00067-3. https://linkinghub.elsevier.com/retrieve/pii/S0034425796000673.

García Criado, M., Myers-Smith, I.H., Bjorkman, A.D., Lehmann, C.E., Stevens, N., 2020. Woody plant encroachment intensifies under climate change across tundra and savanna biomes. Glob. Ecol. Biogeogr. 29, 925–943. https://doi.org/10.1111/geb.13072.

Goulding, H.L., Prowse, T.D., Bonsal, B., 2009. Hydroclimatic controls on the occurrence of break-up and ice-jam flooding in the Mackenzie Delta, NWT. Canada. J. Hydrol. 379, 251–267. https://doi.org/10.1016/j.jhydrol.2009.10.006.

Green, A.A., Berman, M., Switzer, P., Craig, M.D., 1988. A transformation for ordering multispectral data in terms of image quality with implications for noise removal. IEEE Trans. Geosci. Remote Sens. 26, 65–74. https://doi.org/10.1109/36.3001.

Grünberg, I., Wilcox, E.J., Zwieback, S., Marsh, P., Boike, J., 2020. Linking tundra vegetation, snow, soil temperature, and permafrost. Biogeosciences 17, 4261–4279. https://doi.org/10.5194/bg-17-4261-2020.

Hansen, M.C., Potapov, P.V., Moore, R., Hancher, M., Turubanova, S.A., Tyukavina, A., Thau, D., Stehman, S.V., Goetz, S.J., Loveland, T.R., Kommareddy, A., Egorov, A., Chini, L., Justice, C.O., Townshend, J.R.G., 2013. High-resolution global maps of 21st-century forest cover change. Science 342, 850–853. https://doi.org/10.1126/science.1244693. https://www.sciencemag.org/lookup/doi/10.1126/science.1244693.

Hastie, T., Tibshirani, R., Friedman, J., 2009. The Elements of Statistical Learning. volume 103 of Springer Series in Statistics. Springer New York, New York, NY. https://doi.org/10.1007/978-0-387-84858-7. http://link.springer.com/10.1007/978-0-387-84858-7.

He, J., Loboda, T.V., Jenkins, L., Chen, D., 2019. Mapping fractional cover of major fuel type components across Alaskan tundra. Remote Sens. Environ. 232, 111324 https://doi.org/10.1016/j.rse.2019.111324.

Heijmans, M.M.P.D., Magnússon, R., Lara, M.J., Frost, G.V., Myers-Smith, I.H., van Huissteden, J., Jorgenson, M.T., Fedorov, A.N., Epstein, H.E., Lawrence, D.M., Limpens, J., 2022. Tundra vegetation change and impacts on permafrost. Nat. Rev. Earth Environment 3, 68–84. https://doi.org/10.1038/s43017-021-00233-0. https://www.nature.com/articles/s43017-021-00233-0.

Higginbottom, T.P., Symeonakis, E., Meyer, H., van der Linden, S., 2018. Mapping fractional woody cover in semi-arid savannahs using multi-seasonal composites from landsat data. ISPRS J. Photogramm. Remote Sens. 139, 88–102. https://doi.org/10.1016/j.isprsjprs.2018.02.010.

Hu, F.S., Higuera, P.E., Duffy, P., Chipman, M.L., Rocha, A.V., Young, A.M., Kelly, R., Dietze, M.C., 2015. Arctic tundra fires: natural variability and responses to climate change. Front. Ecol. Environ. 13, 369–377. https://doi.org/10.1890/150063.

Huemmrich, K.F., Gamon, J.A., Tweedie, C.E., Campbell, P.K., Landis, D.R., Middleton, E.M., 2013. Arctic tundra vegetation functional types based on photosynthetic physiology and optical properties. IEEE J.Select. Top. Appl.Earth Observ. Remote Sens. 6, 265–275. https://doi.org/10.1109/JSTARS.2013.2253446.

Huete, A., Didan, K., Miura, T., Rodriguez, E., Gao, X., Ferreira, L., 2002. Overview of the radiometric and biophysical performance of the MODIS vegetation indices. Remote Sens. Environ. 83, 195–213. https://doi.org/10.1016/S0034-4257(02)00096-2. https://linkinghub.elsevier.com/retrieve/pii/S0034425702000962.

IPCC, 2021. Climate Change 2021: The Physical Science Basis. Contribution of Working Group I to the Sixth Assessment Report of the Intergovernmental Panel on Climate Change. Technical Report. https://www.ipcc.ch/report/ar6/wg1/.

Jorgenson, J.C., Raynolds, M.K., Reynolds, J.H., Benson, A.M., 2015. Twenty-five year record of changes in plant cover on tundra of northeastern Alaska. Arct. Antarct. Alp. Res. 47, 785–806. https://doi.org/10.1657/AAAR0014-097.

Ju, J., Masek, J.G., 2016. The vegetation greenness trend in Canada and US Alaska from 1984–2012 landsat data. Remote Sens. Environ. 176, 1–16. https://doi.org/10.1016/j.rse.2016.01.001.

Karami, M., Westergaard-Nielsen, A., Normand, S., Treier, U.A., Elberling, B., Hansen, B. U., 2018. A phenology-based approach to the classification of Arctic tundra ecosystems in Greenland. ISPRS J. Photogramm. Remote Sens. 146, 518–529. https://doi.org/10.1016/j.isprsjprs.2018.11.005.

Keshava, N., Mustard, J., 2002. Spectral unmixing. IEEE Signal Process. Magaz. 19, 44–57. https://doi.org/10.1109/79.974727. http://ieeexplore.ieee.org/document/974727/.

Key, C.H., Benson, N.C., 2006. Landscape Assessment: Ground measure of severity, the Composite Burn Index; and Remote sensing of severity, the Normalized Burn Ratio. Technical Report. Ogden, UT. http://pubs.er.usgs.gov/publication/2002085.

Landhausser, S.M., Wein, R.W., 1993. Postfire vegetation recovery and tree establishment at the Arctic treeline: climate-change-vegetation-response hypotheses. J. Ecol. 81, 665–672.

Lantz, T.C., Gergel, S.E., Henry, G.H., 2010a. Response of green alder (Alnus viridis subsp. fruticosa) patch dynamics and plant community composition to fire and regional temperature in North-Western Canada. J. Biogeogr. 37, 1597–1610. https://doi.org/10.1111/j.1365-2699.2010.02317.x.

Lantz, T.C., Gergel, S.E., Kokelj, S.V., 2010b. Spatial heterogeneity in the shrub tundra ecotone in the Mackenzie Delta region, northwest territories: implications for Arctic environmental change. Ecosystems 13, 194–204. https://doi.org/10.1007/s10021-009-9310-0.

Lantz, T.C., Marsh, P., Kokelj, S.V., 2013. Recent shrub proliferation in the Mackenzie Delta uplands and microclimatic implications. Ecosystems 16, 47–59. https://doi.org/10.1007/s10021-012-9595-2.

Lary, D.J., Alavi, A.H., Gandomi, A.H., Walker, A.L., 2016. Machine learning in geosciences and remote sensing. Geosci. Front. 7, 3–10. https://doi.org/10.1016/j.gsf.2015.07.003.

Liljedahl, A.K., Boike, J., Daanen, R.P., Fedorov, A.N., Frost, G.V., Grosse, G., Hinzman, L.D., Iijma, Y., Jorgenson, J.C., Matveyeva, N., Necsoiu, M., Raynolds, M. K., Romanovsky, V.E., Schulla, J., Tape, K.D., Walker, D.A., Wilson, C.J., Yabuki, H., Zona, D., 2016. Pan-Arctic ice-wedge degradation in warming permafrost and its influence on tundra hydrology. Nat. Geosci. 9, 312–318. https://doi.org/10.1038/ngeo2674.

Liljedahl, A.K., Timling, I., Frost, G.V., Daanen, R.P., 2020. Arctic riparian shrub expansion indicates a shift from streams gaining water to those that lose flow. Commun. Earth Environ. 1, 1–9. https://doi.org/10.1038/s43247-020-00050-1.

Loranty, M.M., Goetz, S.J., Beck, P.S.A., 2011. Tundra vegetation effects on pan-Arctic albedo. Environ. Res. Lett. 6, 029601 https://doi.org/10.1088/1748-9326/6/2/029601.

Macander, M.J., Frost, G.V., Nelson, P.R., Swingley, C.S., 2017. Regional quantitative cover mapping of tundra plant functional types in Arctic Alaska. Remote Sens. 9, 1–26. https://doi.org/10.3390/rs9101024.

Martin, A.C., Jeffers, E.S., Petrokofsky, G., Myers-Smith, I., MacIas-Fauria, M., 2017. Shrub growth and expansion in the Arctic tundra: an assessment of controlling factors using an evidence-based approach. Environ. Res. Lett. 12 https://doi.org/10.1088/1748-9326/aa7989.

Maxwell, A.E., Warner, T.A., Fang, F., 2018. Implementation of machine-learning classification in remote sensing: an applied review. Int. J. Remote Sens. 39, 2784–2817. https://doi.org/10.1080/01431161.2018.1433343.

Mcdonald, A.J., Gemmell, F.M., Lewis, P.E., 1996. Investigation of the Utility of Spectral Vegetation Indices for Determining Information on Coniferous Forests. Technical Report.

McManus, K.M., Morton, D.C., Masek, J.G., Wang, D., Sexton, J.O., Nagol, J.R., Ropars, P., Boudreau, S., 2012. Satellite-based evidence for shrub and graminoid tundra expansion in northern Quebec from 1986 to 2010. Global Change Biology 18, 2313–2323. https://doi.org/10.1111/j.1365-2486.2012.02708.x.

Mekonnen, Z.A., Riley, W.J., Grant, R.F., 2018. Accelerated nutrient cycling and increased light competition will Lead to 21st century shrub expansion in North American Arctic tundra. J. Geophys. Res.: Biogeosci. 123, 1683–1701. https://doi.org/10.1029/2017JG004319.

Mekonnen, Z.A., Riley, W.J., Berner, L.T., Bouskill, N.J., Torn, M.S., Iwahana, G., Breen, A.L., Myers-Smith, I.H., Criado, M.G., Liu, Y., Euskirchen, E.S., Goetz, S.J., Mack, M.C., Grant, R.F., 2021. Arctic tundra shrubification: a review of mechanisms and impacts on ecosystem carbon balance. Environ. Res. Lett. 16, 053001 https://doi.org/10.1088/1748-9326/abf28b. https://iopscience.iop.org/article/10.1088/1748-9326/abf28b.

Moffat, N.D., Lantz, T.C., Fraser, R.H., Olthof, I., 2016. Recent vegetation change (1980–2013) in the tundra ecosystems of the Tuktoyaktuk coastlands, NWT, Canada. Arct. Antarct. Alp. Res. 48, 581–597. https://doi.org/10.1657/AAAR0015-063.

Müller, H., Rufin, P., Griffiths, P., Barros Siqueira, A.J., Hostert, P., 2015. Mining dense landsat time series for separating cropland and pasture in a heterogeneous Brazilian savanna landscape. Remote Sens. Environ. 156, 490–499. https://doi.org/10.1016/j.rse.2014.10.014.

Muster, S., Langer, M., Heim, B., Westermann, S., Boike, J., 2012. Subpixel heterogeneity of ice-wedge polygonal tundra: a multi-scale analysis of land cover and evapotranspiration in the Lena River Delta, Siberia. Tellus Ser. B Chem. Phys. Meteorol. 64 https://doi.org/10.3402/tellusb.v64i0.17301.

Myers-Smith, I.H., Hik, D.S., 2018. Climate warming as a driver of tundra shrubline advance. J. Ecol. 106, 547–560. https://doi.org/10.1111/1365-2745.12817.

Myers-Smith, I.H., Forbes, B.C., Wilmking, M., Hallinger, M., Lantz, T., Blok, D., Tape, K. D., MacIas-Fauria, M., Sass-Klaassen, U., Lévesque, E., Boudreau, S., Ropars, P., Hermanutz, L., Trant, A., Collier, L.S., Weijers, S., Rozema, J., Rayback, S.A., Schmidt, N.M., Schaepman-Strub, G., Wipf, S., Rixen, C., Ménard, C.B., Venn, S., Goetz, S., Andreu-Hayles, L., Elmendorf, S., Ravolainen, V., Welker, J., Grogan, P., Epstein, H.E., Hik, D.S., 2011. Shrub expansion in tundra ecosystems: dynamics, impacts and research priorities. Environ. Res. Lett. 6 https://doi.org/10.1088/1748-9326/6/4/045509.

Myers-Smith, I.H., Elmendorf, S.C., Beck, P.S., Wilmking, M., Hallinger, M., Blok, D., Tape, K.D., Rayback, S.A., Macias-Fauria, M., Forbes, B.C., Speed, J.D., Boulanger-Lapointe, N., Rixen, C., Lévesque, E., Schmidt, N.M., Baittinger, C., Trant, A.J., Hermanutz, L., Collier, L.S., Dawes, M.A., Lantz, T.C., Weijers, S., Jørgensen, R.H., Buchwal, A., Buras, A., Naito, A.T., Ravolainen, V., Schaepman-Strub, G., Wheeler, J. A., Wipf, S., Guay, K.C., Hik, D.S., Vellend, M., 2015. Climate sensitivity of shrub growth across the tundra biome. Nature Climate Change 5, 887–891. https://doi.org/10.1038/nclimate2697.

Myers-Smith, I.H., Hallinger, M., Blok, D., Sass-Klaassen, U., Rayback, S.A., Weijers, S., Trant, A.J., Tape, K.D., Naito, A.T., Wipf, S., Rixen, C., Dawes, M.A., Wheeler, J.A., Buchwal, A., Baittinger, C., Macias-Fauria, M., Forbes, B.C., Lévesque, E., Boulanger-Lapointe, N., Beil, I., Ravolainen, V., Wilmking, M., 2015b. Methods for measuring arctic and alpine shrub growth: a review. Earth Sci. Rev. 140, 1–13. https://doi.org/10.1016/j.earscirev.2014.10.004.

Myers-Smith, I.H., Grabowski, M.M., Thomas, H.J., Angers-Blondin, S., Daskalova, G.N., Bjorkman, A.D., Cunliffe, A.M., Assmann, J.J., Boyle, J.S., McLeod, E., McLeod, S., Joe, R., Lennie, P., Arey, D., Gordon, R.R., Eckert, C.D., 2019. Eighteen years of ecological monitoring reveals multiple lines of evidence for tundra vegetation change. Ecol. Monogr. 89 https://doi.org/10.1002/ecm.1351.

Myers-Smith, I.H., Kerby, J.T., Phoenix, G.K., Bjerke, J.W., Epstein, H.E., Assmann, J.J., John, C., Andreu-Hayles, L., Angers-Blondin, S., Beck, P.S., Berner, L.T., Bhatt, U.S., Bjorkman, A.D., Blok, D., Bryn, A., Christiansen, C.T., Cornelissen, J.H.C., Cunliffe, A.M., Elmendorf, S.C., Forbes, B.C., Goetz, S.J., Hollister, R.D., de Jong, R., Loranty, M.M., Macias-Fauria, M., Maseyk, K., Normand, S., Olofsson, J., Parker, T. C., Parmentier, F.J.W., Post, E., Schaepman-Strub, G., Stordal, F., Sullivan, P.F., Thomas, H.J., Tømmervik, H., Treharne, R., Tweedie, C.E., Walker, D.A., Wilmking, M., Wipf, S., 2020. Complexity revealed in the greening of the Arctic. Nat. Clim. Change 10, 106–117. https://doi.org/10.1038/s41558-019-0688-1.

Myneni, R.B., Keeling, C.D., Tucker, C.J., Asrar, G., Nemani, R.R., 1997. Increased plant growth in the northern high latitudes from 1981 to 1991. Nature 386, 698–702. https://doi.org/10.1038/386698a0. http://www.nature.com/articles/386698a0.

Nill, L., Ullmann, T., Kneisel, C., Sobiech-Wolf, J., Baumhauer, R., 2019. Assessing spatiotemporal variations of landsat land surface temperature and multispectral indices in the Arctic Mackenzie Delta region between 1985 and 2018. Remote Sens. 11 https://doi.org/10.3390/rs11192329.

Nitze, I., Grosse, G., 2016. Detection of landscape dynamics in the Arctic Lena Delta with temporally dense landsat time-series stacks. Remote Sens. Environ. 181, 27–41. https://doi.org/10.1016/j.rse.2016.03.038.

Nitze, I., Grosse, G., Jones, B.M., Romanovsky, V.E., Boike, J., 2018. Remote sensing quantifies widespread abundance of permafrost region disturbances across the Arctic and subarctic. Nat.Commun. 9, 1–11. https://doi.org/10.1038/s41467-018-07663-3.

Okujeni, A., van der Linden, S., Tits, L., Somers, B., Hostert, P., 2013. Support vector regression and synthetically mixed training data for quantifying urban land cover. Remote Sens. Environ. 137, 184–197. https://doi.org/10.1016/j.rse.2013.06.007.

Okujeni, A., van der Linden, S., Jakimow, B., Rabe, A., Verrelst, J., Hostert, P., 2014. A comparison of advanced regression algorithms for quantifying urban land cover. Remote Sens. 6, 6324–6346. https://doi.org/10.3390/rs6076324.

Okujeni, A., van der Linden, S., Suess, S., Hostert, P., 2017. Ensemble learning from synthetically mixed training data for quantifying urban land cover with support vector regression. IEEE J. Select. Top. Appl. Earth Observ. Remote Sens. 10, 1640–1650. https://doi.org/10.1109/JSTARS.2016.2634859. http://ieeexplore.ieee.org/document/7792573/https://ieeexplore.ieee.org/document/7792573/.

Okujeni, A., Canters, F., Cooper, S.D., Degerickx, J., Heiden, U., Hostert, P., Priem, F., Roberts, D.A., Somers, B., van der Linden, S., 2018. Generalizing machine learning

regression models using multi-site spectral libraries for mapping vegetation-impervious-soil fractions across multiple cities. Remote Sens. Environ. 216, 482–496. https://doi.org/10.1016/j.rse.2018.07.011.
Okujeni, A., Jänicke, C., Cooper, S., Frantz, D., Hostert, P., Clark, M., Segl, K., van der Linden, S., 2021. Multi-season unmixing of vegetation class fractions across diverse Californian ecoregions using simulated spaceborne imaging spectroscopy data. Remote Sensing of Environment 112558. https://doi.org/10.1016/j.rse.2021.112558. https://linkinghub.elsevier.com/retrieve/pii/S0034425721002789.
Olofsson, P., Foody, G.M., Herold, M., Stehman, S.V., Woodcock, C.E., Wulder, M.A., 2014. Good practices for estimating area and assessing accuracy of land change. Remote Sens. Environ. 148, 42–57. https://doi.org/10.1016/j.rse.2014.02.015.
Olthof, I., Fraser, R.H., 2007. Mapping northern land cover fractions using landsat ETM +. Remote Sens. Environ. 107, 496–509. https://doi.org/10.1016/j.rse.2006.10.009.
Olthof, I., Fraser, R.H., Schmitt, C., 2015. Landsat-based mapping of thermokarst lake dynamics on the Tuktoyaktuk coastal plain, Northwest Territories, Canada since 1985. Remote Sens. Environ. 168, 194–204. https://doi.org/10.1016/j.rse.2015.07.001.
Park, T., Ganguly, S., Tømmervik, H., Euskirchen, E.S., Høgda, K.A., Karlsen, S.R., Brovkin, V., Nemani, R.R., Myneni, R.B., 2016. Changes in growing season duration and productivity of northern vegetation inferred from long-term remote sensing data. Environ. Res. Lett. 11 https://doi.org/10.1088/1748-9326/11/8/084001.
Pearce, C.M., McLennan, D., Cordes, L.D., 1988. The evolution and maintenance of white spruce woodlands on the Mackenzie Delta, N.W.T,Canada. Ecography 11, 248–258. https://doi.org/10.1111/j.1600-0587.1988.tb00807.x.
Peterson, K.M., Billings, W.D., 1980. Arctic and Alpine Research Tundra Vegetational Patterns and Succession in Relation to Microtopography near Atkasook, Alaska Tundra Vegetational Patterns and Succession in Relation to Microtopography Near AtkasooK, Alaska. Arctic Alpine Res. 12, 473–482. https://doi.org/10.1080/00040851.1980.12004207. https://www.tandfonline.com/action/journalInformation?journalCode=uaar20.
Pflugmacher, D., Rabe, A., Peters, M., Hostert, P., 2019. Mapping pan-European land cover using Landsat spectral-temporal metrics and the European LUCAS survey. Remote Sens. Environ. 221, 583–595. https://doi.org/10.1016/j.rse.2018.12.001.
Post, E., Alley, R.B., Christensen, T.R., Macias-Fauria, M., Forbes, B.C., Gooseff, M.N., Iler, A., Kerby, J.T., Laidre, K.L., Mann, M.E., Olofsson, J., Stroeve, J.C., Ulmer, F., Virginia, R.A., Wang, M., 2019. The polar regions in a 2_C warmer world. Sci. Adv. 5 https://doi.org/10.1126/sciadv.aaw9883.
Priem, F., Okujeni, A., van der Linden, S., Canters, F., 2019. Comparing map-based and library-based training approaches for urban land-cover fraction mapping from Sentinel-2 imagery. Int. J. Appl. Earth Obs. Geoinf. 78, 295–305. https://doi.org/10.1016/j.jag.2019.02.003.
Probst, P., Boulesteix, A.L., 2018. To tune or not to tune the number of trees in random forest. J. Mach. Learn. Res. 18, 1–8.
Probst, P., Wright, M.N., Boulesteix, A.L., 2019. Hyperparameters and tuning strategies for random forest. Wiley Interdisc. Rev. Data Mining Knowl. Discovery 9, 1–19. https://doi.org/10.1002/widm.1301.
Rasmussen, C., Williams, C., 2006. Gaussian Processes for Machine Learning. The MIT Press. In: www.GaussianProcess.org/gpml.
Raynolds, M.K., Walker, D.A., Balser, A., Bay, C., Campbell, M., Cherosov, M.M., Daniëls, F.J., Eidesen, P.B., Ermokhina, K.A., Frost, G.V., Jedrzejek, B., Jorgenson, M.T., Kennedy, B.E., Kholod, S.S., Lavrinenko, I.A., Lavrinenko, O.V., Magnússon, B., Matveyeva, N.V., Metúsalemsson, S., Nilsen, L., Olthof, I., Pospelov, I.N., Pospelova, E.B., Pouliot, D., Razzhivin, V., Schaepman-Strub, G., Šibík, J., Telyatnikov, M.Y., Troeva, E., 2019. A raster version of the circumpolar Arctic vegetation map (CAVM). Remote Sens. Environ. 232 https://doi.org/10.1016/j.rse.2019.111297.
Rees, W.G., Hofgaard, A., Boudreau, S., Cairns, D.M., Harper, K., Mamet, S., Mathisen, I., Swirad, Z., Tutubalina, O., 2020. Is subarctic forest advance able to keep pace with climate change? Glob. Chang. Biol. 26, 3965–3977. https://doi.org/10.1111/gcb.15113.
Riihimäki, H., Luoto, M., Heiskanen, J., 2019. Estimating fractional cover of tundra vegetation at multiple scales using unmanned aerial systems and optical satellite data. Remote Sens. Environ. 224, 119–132. https://doi.org/10.1016/j.rse.2019.01.030.
Roberts, D.A., Gardner, M., Church, R., Ustin, S., Scheer, G., Green, R.O., 1998. Mapping chaparral in the Santa Monica Mountains using multiple endmember spectral mixture models. Remote Sens. Environ. 65, 267–279. https://doi.org/10.1016/S0034-4257(98)00037-6.
Ropars, P., Boudreau, S., 2012. Shrub expansion at the foresttundra ecotone: spatial heterogeneity linked to local topography. Environ. Res. Lett. 7 https://doi.org/10.1088/1748-9326/7/1/015501.
Schneider, J., Grosse, G., Wagner, D., 2009. Land cover classification of tundra environments in the Arctic Lena Delta based on Landsat 7 ETM+ data and its application for upscaling of methane emissions. Remote Sens. Environ. 113, 380–391. https://doi.org/10.1016/j.rse.2008.10.013.
Schug, F., Okujeni, A., Hauer, J., Hostert, P., Nielsen, J., van der Linden, S., 2018. Mapping patterns of urban development in Ouagadougou, Burkina Faso, using machine learning regression modeling with bi-seasonal landsat time series. Remote Sens. Environ. 210, 217–228. https://doi.org/10.1016/j.rse.2018.03.022.
Schug, F., Frantz, D., Okujeni, A., van der Linden, S., Hostert, P., 2020. Mapping urban-rural gradients of settlements and vegetation at national scale using Sentinel-2 spectral-temporal metrics and regression-based unmixing with synthetic training data. Remote Sens. Environ. 246, 111810 https://doi.org/10.1016/j.rse.2020.111810, doi:10.1016/j.rse.2020.111810.
Schwieder, M., Leitão, P.J., da Cunha Bustamante, M.M., Ferreira, L.G., Rabe, A., Hostert, P., 2016. Mapping Brazilian savanna vegetation gradients with Landsat time series. Int. J. Appl. Earth Obs. Geoinf. 52, 361–370. https://doi.org/10.1016/j.jag.2016.06.019.
Scott, P.A., Hansell, R.I.C., 2002. Development of White Spruce Tree Islands in the Shrub Zone of the Forest-Tundra. Arctic 55, 238–246. http://www.jstor.org/stable/40512469.
Seider, J.H., Lantz, T.C., Hermosilla, T., Wulder, M.A., Wang, J.A., 2022. Biophysical determinants of shifting Tundra vegetation productivity in the beaufort delta regionof Canada. Ecosystems 1–20. https://doi.org/10.1007/S10021-021-00725-6/FIGURES/8.
Selkowitz, D.J., 2010. A comparison of multi-spectral, multi-angular, and multi-temporal remote sensing datasets for fractional shrub canopy mapping in Arctic Alaska. Remote Sens. Environ. 114, 1338–1352. https://doi.org/10.1016/j.rse.2010.01.012.
Senf, C., Lastovicka, J., Okujeni, A., Heurich, M., van der Linden, S., 2020. A generalized regression-based unmixing model for mapping forest cover fractions throughout three decades of Landsat data. Remote Sens. Environ. 240 https://doi.org/10.1016/j.rse.2020.111691.
Serreze, M.C., Barry, R.G., 2011. Processes and impacts of Arctic amplification: A research synthesis. Global Planetary Change 77, 85–96. https://doi.org/10.1016/j.gloplacha.2011.03.004.
Settle, J.J., Drake, N.A., 1993. Linear mixing and the estimation of ground cover proportions. 14, 1159–1177. https://doi.org/10.1080/01431169308904402.
Snoek, J., Larochelle, H., Adams, R.P., 2012. Practical Bayesian Optimization of Machine Learning Algorithms.
Stewart, L., Simonsen, C.E., Svenning, J.C., Schmidt, N.M., Pellissier, L., 2018. Forecasted homogenization of high Arctic vegetation communities under climate change. J. Biogeogr. 45, 2576–2587. https://doi.org/10.1111/jbi.13434.
Suess, S., van der Linden, S., Okujeni, A., Griffiths, P., Leitão, P.J., Schwieder, M., Hostert, P., Leitao, P.J., Schwieder, M., Hostert, P., Leitão, P.J., Schwieder, M., Hostert, P., Leitao, P.J., Schwieder, M., Hostert, P., 2018. Characterizing 32 years of shrub cover dynamics in southern Portugal using annual landsat composites and machine learning regression modeling. Remote Sens. Environ. 219, 353–364. https://doi.org/10.1016/j.rse.2018.10.004.
Tape, K., Sturm, M., Racine, C., 2006. The evidence for shrub expansion in northern Alaska and the pan-Arctic. Glob. Chang. Biol. 12, 686–702. https://doi.org/10.1111/j.1365-2486.2006.01128.x.
Timoney, K.P., La Roi, G.H., Zoltai, S.C., Robinson, A.L., 1992. The high subarctic forest-tundra of northwestern Canada: position, width, and vegetation gradients in relation to climate. Arctic 45, 1–9. https://doi.org/10.14430/arctic1367.
Tucker, C.J., 1979. Red and photographic infrared linear combinations for monitoring vegetation. Remote Sens. Environ. 8, 127–150. https://doi.org/10.1016/0034-4257(79)90013-0.
U.S. Geological Survey, 2021. Landsat Collection 2 (ver. 1.1, January 15, 2021). Technical Report. Reston, VA. https://doi.org/10.3133/fs20213002.
Venter, Z.S., Cramer, M.D., Hawkins, H.J., 2018. Drivers of woody plant encroachment over Africa. Nat. Commun. https://doi.org/10.1038/s41467-018-04616-8.
Viereck, L.A., Werdin-Pfisterer, N.R., Adams, P.C., Yoshikawa, K., 1981. Effect of wildfire and fireline construction on the annual depth of thaw in a black spruce permafrost forest in Interior Alaska: A 36-year record of recovery. In: Proceedings of the Ninth International Conference on Permafrost. June 29-July 3, 2008; Fairbanks, AK, 1845–1850.
Wang, J.A., Sulla-Menashe, D., Woodcock, C.E., Sonnentag, O., Keeling, R.F., Friedl, M.A., 2020. Extensive land cover change across Arctic-boreal northwestern North America from disturbance and climate forcing. Glob. Chang. Biol. 26, 807–822. https://doi.org/10.1111/gcb.14804.
Wulder, M.A., Loveland, T.R., Roy, D.P., Crawford, C.J., Masek, J.G., Woodcock, C.E., Allen, R.G., Anderson, M.C., Belward, A.S., Cohen, W.B., Dwyer, J., Erb, A., Gao, F., Griffiths, P., Helder, D., Hermosilla, T., Hipple, J.D., Hostert, P., Hughes, M.J., Huntington, J., Johnson, D.M., Kennedy, R., Kilic, A., Li, Z., Lymburner, L., McCorkel, J., Pahlevan, N., Scambos, T.A., Schaaf, C., Schott, J.R., Sheng, Y., Storey, J., Vermote, E., Vogelmann, J., White, J.C., Wynne, R.H., Zhu, Z., 2019. Current status of landsat program, science, and applications. Remote Sens. Environ. https://doi.org/10.1016/j.rse.2019.02.015.
Xu, H., 2006. Modification of normalised difference water index (NDWI) to enhance open water features in remotely sensed imagery. Int. J. Remote Sens. 27, 3025–3033. https://doi.org/10.1080/01431160600589179.
Zhu, Z., Wulder, M.A., Roy, D.P., Woodcock, C.E., Hansen, M.C., Radeloff, V.C., Healey, S.P., Schaaf, C., Hostert, P., Strobl, P., Pekel, J.F., Lymburner, L., Pahlevan, N., Scambos, T.A., 2019. Benefits of the free and open landsat data policy. Remote Sens. Environ. 224, 382–385. https://doi.org/10.1016/j.rse.2019.02.016.